

Optimization of Hydrophobic Meshes for Oil Spill Recovery

by

Daniel P. Prendergast

Sc.B. Chemical Engineering

Brown University, 2011

Submitted to the Department of Civil and Environmental Engineering
in partial fulfillment of the requirements for the degree of

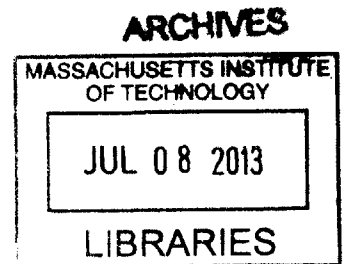
MASTER OF SCIENCE IN CIVIL AND ENVIRONMENTAL ENGINEERING

at the

MASSACHUSETTS INSTITUTE OF TECHNOLOGY

June 2013

© 2013 Massachusetts Institute of Technology. All rights reserved.



Author.....

Department of Civil and Environmental Engineering

May 10, 2013

Certified by.....

Philip M. Gschwend

Professor of Civil and Environmental Engineering

Thesis Supervisor

Accepted by.....

Heidi M. Nepf

Chair, Departmental Committee for Graduate Students

Optimizing Hydrophobic Meshes for Oil Spill Recovery

by

Daniel P. Prendergast

Submitted to the Department of Civil and Environmental Engineering
on May 10, 2013 in Partial Fulfillment of the
Requirements for the Degree of Master of Science in
Civil and Environmental Engineering

ABSTRACT

Widespread use of petrochemicals often leads to accidental releases in aquatic environments, occasionally with disastrous results. Recent advances in the understanding of selectively wetting surfaces have led to the development of functionalized steel meshes with hydrophobic and oleophilic surfaces. These meshes can perform oil/water separation *in situ*, continuously, via capillary action. The goal of this study is to determine the potential of hydrophobic meshes as oil spill recovery devices. A fabrication method was developed using steel mesh dip-coated in a hot solution of low-density polyethylene (LDPE) in xylene. The mesh gained a rough, hydrophobic coating of LDPE, with tunable pore sizes and surface roughness. The coating was characterized using microscopy techniques and contact angle analysis, in order to identify surface features relevant to oil/water separation. Oil was found to persistently wet the mesh, attenuating any effects from roughness. Next, a key performance metric, the water breakthrough pressure, was predicted using a modified version of the Young-Laplace equation incorporating an unpinned meniscus. The model was successful for meshes with pore radii between 7 – 220 μm , which could hold back up to 40 cm of water. Finally, a bench-scale apparatus was built to test the oil permeate flux at steady state under capillary-driven flow. The mesh successfully recovered oil from the surface of a pool of water, with less than 1% water recovered by mass, with a representative flux of 1 $\text{L}\cdot\text{m}^{-2}\cdot\text{s}$. These results were used to discuss implications for the feasibility of field-scale devices.

Thesis Supervisor: Philip M. Gschwend

Title: Professor of Civil and Environmental Engineering

Acknowledgements

First and foremost, I am deeply grateful to my advisor, Phil Gschwend, for his encouragement, creativity, and inexhaustible energy. I'd also like to thank my collaborators Da Deng and Francesco Stellacci for their expertise and contributions to this work. Together, they developed the technique of coating mesh with LDPE, and Da provided the SEM images. This work also made use of the MRSEC Shared Experimental Facilities at MIT, supported by the National Science Foundation under award number DMR-08-19762. I thank Prof. Roman Stocker for the use of his optical microscopes. I'm grateful to Eni S.p.A. for funding this endeavor, especially Roberto Bagatin and Francesca Rubertelli.

Many other people deserve thanks and recognition: my labmates (John, Dave, Patricia, Jenn, and Jordan) for their good humor and generous advice, my friends in the Parsons community for keeping my workplace enjoyable, and finally, my family for their love and support.

Table of Contents

Chapter 1 – Introduction	11
1.1 Oil Spill Fate and Effects	11
1.2 Remediation Technologies.....	13
1.3 Objective	15
1.4 References.....	16
Chapter 2 – Hydrophobic Mesh Fabrication and Characterization	19
2.1 Introduction	19
2.2 Theory	20
2.3 Methods	22
2.4 Results and Discussion.....	25
2.5 Conclusions.....	35
2.6 References.....	36
Chapter 3 – Water Breakthrough Pressure	39
3.1 Introduction	39
3.2 Theory	40
3.3 Methods	43
3.4 Results and Discussion.....	44
3.5 Conclusions.....	48
3.6 References.....	49
Chapter 4 – Oil Permeate Flux	51
4.1 Introduction	51
4.2 Theory	52
4.3 Methods	53
4.4 Results and Discussion.....	57
4.5 Conclusions.....	60
4.6 References.....	61
Conclusions & Future Work	63
Appendix	67

List of Figures

- Figure 2.1:** Inverse optical microscopy images of stainless steel mesh with uncoated opening widths of: (1) 100 μm , (2) 220 μm , and (3) 1500 μm . Coating concentrations are (A) uncoated, (B) 15 mg LDPE / mL xylene; (C) 30 mg LDPE / mL xylene; (D) 60 mg LDPE / mL xylene. 26
- Figure 2.2:** Scanning electron microscopy images of stainless steel mesh with an uncoated opening width of 220 μm at varying coating concentrations and magnifications. Coating concentrations are: (1) 15 mg LDPE / mL xylene; (2) 30 mg LDPE / mL xylene; (3) 60 mg LDPE / mL xylene, and magnifications are (A) $\times 95$; (B) $\times 1600$; (C) $\times 13000$. 27
- Figure 2.3:** Scanning electron microscopy images of stainless steel mesh coated with a 60 mg LDPE / mL xylene solution at varying mesh sizes and magnifications. Uncoated mesh opening widths are (A) 100 μm and (B) 1500 μm . Magnifications are (1) $\times 95$; (2) $\times 1600$; (3) $\times 13000$. 28
- Figure 2.4:** Measured water contact angles on stainless steel meshes coated in various concentrations of LDPE-xylene solutions. Mesh size refers to the width of the uncoated openings. Both the coating thickness and roughness increased with solution concentration. 32
- Figure 2.5:** SEM images of a 100 μm mesh with a 60 mg/mL LDPE-xylene coating before (a, b) and after (c, d) separating crude oil and rinsing with dichloromethane. 33
- Figure 2.6:** Olive oil wetting a 100 μm mesh coated with a 60 mg/mL LDPE-xylene solution. The oil fills the interstitial spaces of the mesh (a), making the surface much smoother (b). 34
- Figure 3.1:** Cross-section of the water meniscus suspended within an idealized coated mesh opening. As the water column height above the meniscus changes, the contact point (located by the angle from the horizontal φ) moves up or down the surface of the wire, while maintaining a constant contact angle θ relative to the local tangent. 42
- Figure 3.2:** Comparison of the observed breakthrough heights and those predicted by two models: the classic capillary height equation and one modified from Liu and Lange⁷. Error bars represent experimental precision for the observed values, and propagation of variance from average pore size calculations for the predictions. 45

Figure 3.3: Breakthrough depths of various mesh geometries. Predicted height is based on a model derived from Liu and Lange⁷. Error bars represent experimental precision for the observed values, and propagation of variance from average pore size calculations for the prediction. 47

Figure 4.1: Photos and diagram of initial recovery apparatus. Center: illustration showing the integrated collection system recovering oil; blue represents seawater, black represents a crude oil spill. Left: photo of the test tube with windows cut in its side covered with a LDPE-coated mesh. This tube was lowered into beakers with floating oil. The oil passed through the mesh and was continuously pumped to an external reservoir. Right: photo showing the system during operation. Oil removal occurred on the sides of the device with mesh (left and right in the photo), but not elsewhere (e.g., bottom of photo). 55

Figure 4.2: Steady-state apparatus design, with return flow to ensure a constant supply of oil in the beaker. Left: Diagram of the apparatus, where blue is water and black is oil. Right: Photo of the mesh incorporated into the apparatus. The olive oil is yellow, and both can be seen in contact with the mesh surface. Process: (1) Mesh separates the oil and water; (2) Oil permeate is collected and removed from the recover device (3) Oil permeate is returned to the floating oil. 56

Figure 4.3: Comparison of predicted and observed olive oil permeate flux through hydrophobic mesh of varying sizes. Error bars represent experimental precision and propagation of uncertainty in pore geometry for the observed and predicted fluxes, respectively. 58

Figure 4.4: Comparison of predicted and observed oil permeate flux through a single mesh with coated dimensions of $r = 55 \mu\text{m}$, and $R = 167 \mu\text{m}$. Coating concentration was 60 mg LDPE / mL xylene. 59

List of Tables

Table 2.1: Crystallinity of LDPE coated on a 220 μm mesh.....	30
Table 2.2: Roughness parameters of the 220 μm mesh with various coatings.....	31
Table 4.1: Physical properties of oils tested with oil-water separation device.....	54
Table A.1: Dimensions of coated and uncoated meshes used in Chapter 2 and 3, identified by uncoated opening width.....	67
Table A.2: Dimensions of coated meshes used in Chapter 3 and 4, identified by mesh dimensions.....	67

Chapter 1 – Introduction

1.1 Oil Spill Fate and Effects

All too commonly, human activities pollute aquatic environments with petroleum products from a variety of sources, including extraction wells, tankers, storage facilities, and refineries.¹ Fortunately, spill frequency and volume from all international sources have decreased since the 1970's due to increasing implementation of preventative regulations and the actions of the oil production and transportation industries.² However, while the average spill volume has decreased, catastrophically large spills still occur at intervals, sharply deviating from the overall trend. One example is the 2010 Deepwater Horizon incident in the Gulf of Mexico which released an estimated 4.1 million barrels of crude oil from approximately 66 km off the Louisiana shore.³ The cost of the oil spill, including the damage to the coastal ecosystem and the loss of an entire fishing and tourism season, is still being tabulated. The failure to prevent crude oil from reaching sensitive areas increased damages, drew widespread public attention, and highlighted the need for new technological approaches to oil spill remediation.

Oil spills are an extremely complex contamination event to understand and remediate. Crude oil consists of more than 10^5 individual compounds,⁴ most of which are hydrocarbons with a relatively small fraction of heteroatomic compounds. Every single component is affected by the environment individually, while influencing the properties of the mixture as a whole. Processed petroleum products, such as diesel fuel or bunker fuel, commonly consist of a certain portion of the crude oil composition, typically related by boiling point.⁵ Because they only

possess a subset of the compounds found in crude oil, processed fuels may have significantly different behavior during a spill.

After release to an aquatic environment, oil undergoes numerous processes collectively known as “weathering” that alter its composition and fate.⁶ An oil slick both moves with the underlying water currents and spreads relative to the water surface.⁷ Spreading broadens and thins the oil slick at a rapid rate controlled by gravity and the oil viscosity.⁸ As it is exposed to wind and wave action, the oil is transferred to the air *via* evaporation, which favors the lighter components.⁹ Simultaneously, oil will dissolve into the water column, which favors the lighter polar compounds.¹⁰ Both of these processes cause the remaining oil to become enriched with heavier, apolar compounds, which increases the viscosity of the slick. Depending on the composition of the oil, the depletion of lighter compounds can enhance the transformation of a slick into a water-in-oil emulsion through wind and wave action.¹¹ Eventually, the oil can become so entrained with water (up to 80% by volume), it breaks up into neutrally buoyant “tar balls”, causing it to sink and be transported hundreds of miles with prevailing currents.¹² Oil on the surface can undergo photodegradation¹³ where it is broken down into smaller components or transformed into oxygenated compounds.¹⁴

The impact of oil on the environment is largely felt through its toxicity to aquatic fauna. Oil can be broken down by native microbial life through biodegradation,¹⁵ but a spill often causes local concentrations to reach toxic levels. The two major known mechanisms of oil toxicity are nonspecific narcosis,¹⁶ where the compounds partition into cell membranes and disrupt critical transport processes, and specific carcinogenic activity of individual species such

as polycyclic aromatic hydrocarbons.¹⁷ The bioavailability of these compounds is largely determined by their solubility,¹⁶ but there is some evidence that even the least soluble compounds can have a long-term detrimental effect on local organisms.¹⁸ The uncertainty associated with toxic effects can be significant, making our knowledge of how oil impacts the environment largely incomplete.

With respect to remediation, spilled oil is best amenable to treatment as early as possible.¹⁹ Depending on the wind speed, oil composition, and other factors, floating oil emulsifies within hours to days, drastically reducing the efficiency of all treatment methods.²⁰ Oil that is evaporated into the atmosphere, or dissolved or dispersed as droplets into the water column is essentially beyond the reach of treatment,¹⁹ and will remain in the environment until broken down naturally. Therefore, for all spills, there is only a narrow window where cleanup is feasible. For large volume spills, assembling and utilizing the proper equipment during this window becomes a formidable challenge.

1.2 Remediation Technologies

Current technologies used to cleanup oil spills can be broadly classified into two groups: destructive methods and recovery methods. Destructive methods ensure the oil is no longer a consistent slick, but prevent any possibility of recovery. For example, *in-situ* burning involves corralling a slick using floating boom in order to thicken the oil, followed by a controlled burning of the oil.²¹ Dispersants are chemical surfactants sprayed onto an oil slick from boats or aircraft. The surfactants promote the formation of small oil droplets, which enhances the natural biodegradation rate²² as the droplets are entrained in the water column. Both of these methods

can remediate oil quickly, but their full environmental impact is unknown. Along with bioremediation, which is the addition of nutrients or specialized microbes to promote biodegradation,¹⁵ oil treated with these methods is transformed, but not removed from the environment.

Common recovery methods include skimmers and sorbents. Skimmers are a broad category of stationary or mobile mechanical devices specifically designed to recover oil from the water's surface.²³ To separate the water and oil, they typically take advantage of the difference in density or adhesive properties between oil and water. Sorbents selectively soak up oil in the presence of water, and can often be reused after treatment.²⁴ Unfortunately, the recovery rate and efficiency of skimmers declines rapidly in moderate waves and currents, and must be deployed from a vessel.²³ Sorbents can be spread over a large area autonomously, but have a finite recovery capacity and are difficult to handle safely when soaked in oil.²⁴ These current limitations provide motivation for developing new oil spill recovery technologies.

An emerging approach to oil-water separations is to imbue inexpensive, durable substrates with selectively wetting surfaces. In 2004, Feng et al.²⁵ coated a stainless steel mesh by spraying it with a polytetrafluoroethylene (PTFE) emulsion. The PTFE coated mesh resisted wetting by water, but was completely wetted by nonpolar, low surface energy oils, making it hydrophobic and oleophilic. A falling oil droplet was observed to rapidly pass through the mesh, which led to the conclusion that separation of oil and water using a selectively wetting mesh was feasible. Numerous proof-of-concept separations have since been performed using metallic meshes whose surfaces have been functionalized to be hydrophobic and oleophilic.

Hydrophobic meshes are a promising new approach to oil spill remediation. They have been shown to separate oil from water *in-situ*, continuously, and without any energy input besides pumping away the recovered oil. Many methods have recently been developed to functionalize the surface of a steel mesh, but it is unclear if these surfaces can withstand the rigors of a marine environment. In addition, there have been comparatively few investigations into the ability of these meshes to reject water and the rate at which oil can be recovered.

1.3 Objective

The purpose of this work is to investigate the underlying parameters of hydrophobic meshes that govern performance as an oil/water separation technique in order to fully assess their potential for oil spill recovery devices. Chapter 2 describes the development of a fabrication technique for a hydrophobic mesh ideally suited as a testing system. The coated mesh is characterized using various microscopy techniques, and the surface characteristics most relevant to oil/water separation are explored and discussed. Chapter 3 introduces the theoretical modeling of water intrusion, and uses a modified model to predict the depth at which the mesh can be submerged before undesired water begins to permeate. In Chapter 4, a bench-scale apparatus incorporating the hydrophobic mesh is developed and successfully used to separate a variety of oils floating in a container of water. The apparatus is used to investigate influence of mesh geometry and surface characteristics on the rate of oil flux, which is compared to predictions from simple capillary theory. This thesis concludes with recommendations for optimally implementing this mesh as a field-scale oil spill recovery device.

1.4 References

- (1) Vanem, E.; Endresen, Ø.; Skjong, R. *Reliab. Eng. Syst. Saf.* **2008**, *93*, 1354-1368.
- (2) Burgherr, P. *J. Hazard. Mater.* **2007**, *140*, 245-256.
- (3) Camilli, R.; Di Iorio, D.; Bowen, A.; Reddy, C. M.; Techet, A. H.; Yoerger, D. R.; Whitcomb, L. L.; Seewald, J. S.; Sylva, S. P.; Fenwick, *Proc. Natl. Acad. Sci. U. S. A.* **2011**, *109* (50), 20260-20267.
- (4) Rodger, R.P.; McKenna, A.M. *Anal. Chem.* **2011**, *83*, 4665-4687.
- (5) Speight, J.G. *The Chemistry and Technology of Petroleum*, 4th ed.; CRC Press: Boca Raton, 2007; pp 853-855.
- (6) Jordan, R.E.; Payne, J.R. *Fate and Weathering of Petroleum Spills in the Marine Environment*; Ann Arbor Science Publishers, Inc.: Ann Arbor, MI, 1980; p 5.
- (7) Fay, J.A. Physical processes in the spread of oil on a water surface. In *Proceedings, Joint Conference and Control of Oil Spills*, June 15–17, Washington, DC, 1971.
- (8) McAuliffe, C.D. Organism exposure to volatile/soluble hydrocarbons from crude oil spills—A field and laboratory comparison. *Proceedings, 1987 Oil Spill Conference*, Baltimore, MD, USA, April 6–9, 1987. American Petroleum Institute, Washington, DC, pp 275–288.
- (9) Mackay, D.; Matsugu, R.S. *Can J Chem Eng* **1973**, *51*, 434–439.
- (10) Arey, J.S.; Nelson, R.K.; Reddy, C.M. *Environ. Sci. Technol.* **2007**, *41*, 5738-5746.
- (11) Fingas, M. *Spill Sci. Technol. Bull.* **1995**, *2*, 55–59.
- (12) Reed, M.; Johansen, Ø; Brandvik, P.J.; Daling, P.; Lewis, A.; Fiocco, R.; Mackay, D.; Prentki, R. *Spill Sci. Technol. Bull.* **1999**, *5*(1), 3-16.
- (13) Plata, D.L.; Sharpless, C.M.; Reddy, C.M. *Environ. Sci. Technol.* **2008**, *42*, 2432-2438.
- (14) Aeppli, C.; Carmichael, C.A.; Nelson, R.K.; Lemkau, K.L.; Graham, W.M.; Redmond, M.C.; Valentine, D.L.; Reddy, C.M. *Environ. Sci. Technol.* **2012**, *46*, 8799-8807.
- (15) Atlas, R.M. *Mar. Pollut. Bull.* **1995**, *31*(4), 178-182.

- (16) Tcaciuc, A.P.; Nelson, R.K.; Reddy, C.M.; Gschwend, P.M. *Environ. Sci. Technol.* **2012**, *46*, 3449-3456.
- (17) Swartz R.C.; Schults D.W.; Ozretich, R.; Lamberson, J.; Cole, F.; DeWitt, T.; Redmond, M.; Ferraro, S.; *Environ. Toxicol. Chem.* **1995**, *14*, 1977-1987.
- (18) Carls, M.G.; Rice, S.D.; Hose, J.E. *Environ. Toxicol. Chem.* **1999**, *18*, 481-493.
- (19) Nordvik, A.B. *Spill Sci. Technol. Bull.* **1995**, *2(1)*, 17-46.
- (20) Daling, P.S.; Brandvik, P.J.; Mackay, D.; Johansen, O. *Oil Chem. Pollut.* **1990**, *7(3)*, 173-198.
- (21) Buist, I.; McCourt, J.; Potter, S.; Ross, S.; Trudel, K. *Pure Appl. Chem.* **1999**, *71(4)*, 3-65.
- (22) Lessard, R.R.; Demarco, G. *Spill Sci. Technol. Bull.* **2000**, *6*, 59-68.
- (23) Schulze, R. *Oil Spill Response Performane Review of Skimmers*; ASTM: Scranton, PA, 1994; Vol. 34.
- (24) Adebajo, M.O.; Frost, R.L.; Kloprogge, J.T.; Carmody, O.; Kokot, S. *J. Porous Mater.* **2003**, *10*, 159-170.
- (25) Feng, L.; Zhang, Z.; Mai, Z.; Ma, Y.; Liu, B.; Jiang, L.; Zhu, D. *Angew. Chem., Int. Ed.* **2004**, *43*, 2012-2014.

Chapter 2 – Hydrophobic Mesh Fabrication and Characterization

2.1 Introduction

Fabrication methods of hydrophobic/oleophilic meshes are numerous, and include electrospinning or airbrushing polymer coatings,^{1,2,3} inducing the growth of carbon nanotubes,^{4,5} chemical etching,^{6,7} growing fluorinated zinc oxide crystals,⁸ and self-assembly of long-chain fatty acids.⁹ Additionally, hydrophilic/oleophobic metallic meshes can separate oil and water by allowing the passage of water while preventing the flow of oil; such surfaces have been created by photoinitiated polymerization of hydrogel coatings,¹⁰ solution grafting of perfluorinated polyethylene glycol surfactants¹¹ and spray coating nanoparticle-polymer suspensions.¹² This technique of functionalizing surfaces has also been extended to sorbents: Yuan et al.¹³ coated a paper-like nanowire substrate with polydimethyl siloxane (PDMS). The coating both enhanced its hydrophobicity and markedly improved its ability to selectively absorb oil, even in presence of large water quantities. Unfortunately, none of the above methods create a surface that is clearly both durable and economic to produce. In addition, quantitative analysis of the separation capabilities of the functionalized meshes has been limited.¹⁴

Recently, Deng et al.¹⁵ developed a method to create a hydrophobic/oleophilic mesh using a one-step dip coating process. By dissolving low-density polyethylene (LDPE) in a hot xylene solution, steel mesh could be coated in rough LDPE, creating a mesh with both a hydrophobic surface and a mechanically strong substrate. The materials consumed in the

fabrication process consist of only stainless steel and LDPE, which are both commercially available and inexpensive. The two materials are unlikely to impact the environment, and are durable enough to withstand the rigors of deployment in a marine environment. Taken all together, this type of hydrophobic mesh is a favorable candidate for use in the cleanup of oil spills. The goal of this work is to systematically alter the fabrication process to achieve desired surface characteristics, and link those surface properties to performance metrics relevant to oil spill remediation.

2.2 Theory

The wetting of a solid surface by a liquid is described with the classical Young's equation¹⁶ (Equation 2.1). It predicts the local contact angle of the edge of a droplet when gravitational forces can be neglected (generally when the radius of the drop is smaller than the characteristic capillarity length, which is about 2 mm at standard conditions¹⁷):

$$\cos \theta = (\gamma_{SG} - \gamma_{SL}) / \gamma_{LG} \quad (2.1)$$

where θ is the local contact angle, and γ_{SG} , γ_{SL} , and γ_{LG} are the surface tensions of the solid-gas, solid-liquid, and liquid-gas interfaces. This local contact angle determines whether the liquid "wets" or does not wet the surface. A wetting liquid is generally described as one with a local contact angle of less than 90° , and a non-wetting liquid as one which has a local contact angle of greater than 90° . Specifically, a surface is known as "hydrophobic" if it is not wetted by water, and "hydrophilic" if it is. Since Young's equation represents the balance of forces exerted by surface tensions at the edge of the drop, this contact angle determines a myriad of

hydrodynamic phenomena, including the spontaneous spreading of the liquid over the surface, capillary action, and many others.

Young's Equation only applies to anisotropic, smooth surfaces. To account for non-idealities or a rough surface composed of LDPE, a model based on the Cassie-Baxter equation¹⁸ is used

$$\cos \theta^* = r_f f \cos \theta + f - 1 \quad (2.2)$$

where θ^* is the apparent water contact angle of the composite surface, f is the area fraction of the projection of the LDPE in contact with the liquid, r_f is the roughness ratio of the part of the LDPE surface that is wet by the liquid (ratio of actual surface area to apparent surface area), and θ is the contact angle of water on a smooth LDPE surface. Note that increasing the roughness ratio for a hydrophobic surface ($\theta > 90^\circ$) increases the apparent contact angle, and decreases the apparent contact angle for hydrophilic surfaces. In addition, for either type of surface, decreasing the fraction of solid in contact with the liquid will increase the apparent contact angle, as the contact angle of any liquid with air is assumed to be 180° .¹⁹ This fraction of air affects the value of f through both the openings in the mesh, and any partial wetting of the LDPE surface resulting from incomplete wetting of submicron structures.

These previous results are the product of a recent string of theoretical and practical innovations in the field of material science.²⁰ Efforts in understanding the fundamental parameters that govern surface characteristics have led to striking outcomes, including the creation of "superhydrophobic" surfaces: those with water contact angles of 150° or greater.²⁰

These surfaces are best achieved with roughness on multiple length scales (e.g. overlapping protrusions of both 10^{-6} and 10^{-9} m in length). Thus, a thorough characterization of the mesh surface will provide a foundation for determining the maximum potential performance of the mesh as an oil/water separator.

2.3 Methods

Materials. All materials were used as received. Low-density polyethylene (LDPE) was obtained as pellets from Aldrich and had a melt flow index of $2.8 \text{ g}\cdot\text{min}^{-1}$ at 190°C . Woven stainless steel (304) meshes were obtained from McMaster-Carr with three opening sizes: $100 \mu\text{m}$, $220 \mu\text{m}$, and $1500 \mu\text{m}$. All meshes were cleaned three times in an ultrasonic bath with a 50:50 ethanol:water solution for 5 min before use. ACS reagent-grade mixed-isomer xylenes were obtained from Sigma-Aldrich.

Mesh Fabrication. The desired mass of LDPE was dissolved in the mixed-isomer xylenes at 110°C while stirring. Concentrations of LDPE in xylene used in these experiments were limited to $15 \text{ mg}\cdot\text{mL}^{-1}$, $30 \text{ mg}\cdot\text{mL}^{-1}$, and $60 \text{ mg}\cdot\text{mL}^{-1}$. Then, a sample of the woven stainless steel mesh was soaked in the dissolved LDPE solution for 30 min to enable adhering air bubbles to escape. Subsequently, the mesh was removed fully wetted, kept in a horizontal position, and air-dried in a fume hood at room temperature on a wire scaffold. After air-drying for 30 min, the coated mesh was heated in a ventilated oven at 70°C overnight.

Characterization of Meshes Using Optical Microscopy. Physical dimensions of the coated and uncoated meshes were measured using an inverted optical microscope (TE2000;

Nikon). First, the areas of a large sampling of openings for each mesh-coating combination were measured and the mean area was calculated. Then, this mean area was used to calculate an effective pore radius r of a circle with equivalent area. The corresponding effective coated wire radius R was calculated by halving the width of an uncoated mesh opening, subtracting the effective pore radius, and adding the radius of the uncoated wire. An exception was made for meshes coated with a 15 mg·mL⁻¹ LDPE-xylene solution, since using this method would result in an effective coated wire radius smaller than the radius of an uncoated wire. In that case, the coated wire radius R was measured directly. A summary of these coated-mesh properties can be found in Appendix Table A.1.

SEM Images. The micro- and nano-scale morphology of the LDPE coating was revealed using a field emission scanning electron microscope (SEM, JEOL) operating at 15 kV. Before FESEM observations, the samples were coated with gold to improve their surface conductivity by a gold sputter (EffaCoater) at 30 mA for 30 seconds in vacuum.

Crystallinity Measurements. The crystallinity of the LDPE coating was assessed using a power compensated differential scanning calorimeter (Diamond; Perkin Elmer) to measure the enthalpy of fusion. The temperature program consisted of: (1) Ramp from 50°C to 80°C at 20°C/min; (2) Isothermal hold for 1 min at 80°C; (3) Ramp to 150°C at 20°C/min; (4) Isothermal hold at 150°C for 1 min; (5) Ramp to 50°C at 20°C/min; (6) Isothermal hold at 50°C for 1 min; (7) Cool to 50°C at 20°C/min. Reported values are calculated after subtracting a background uncoated mesh sample. The reported percent crystallinity values are an average of three runs calculated using a value of 290 J/g for fully crystalline LDPE²¹.

Reported uncertainty reflects error in experimental accuracy, which was larger than the observed variance.

AFM Roughness Measurements. The roughness of a 10 μm by 10 μm area of the coated meshes was determined by probing the surface topography using an atomic force microscope (D3100, Nanoscope IIIa controller; Veeco/Digital Instruments, Santa Barbara, CA, USA). Due to the inherent curvature of the woven wire substrate, and the large size of the LDPE surface microstructures (commonly greater than 5 μm), the roughness ratio (ratio of the actual surface area to the projected surface area) could only be calculated for the most raised portion of the wires, which were relatively uncoated compared to the remainder of the mesh. Further discussion regarding this limitation can be found in Section 2.4.

SEM Roughness Index. To supplement the AFM roughness measurements, the SEM images were analyzed using an image processing technique. The image is converted to greyscale, and each of the pixels in the image is assigned a value from 0-255, corresponding to its position in the greyscale spectrum. These values roughly correspond to height in an SEM image. The SEM roughness index is equal to the standard deviation of the number distribution of these values within a given area or line on the image. It is a relative measure of roughness, with rougher surfaces having a larger index.

Contact Angle Measurements. Water contact angle measurements were made using 10 μL drops of distilled water at three different spots on each sample. Drop images were captured using a digital SLR camera (EOS Rebel XSi; Canon) fitted with a macro lens (EF 50mm f/2.5 Compact Macro). The contact angle was determined from image data using software

developed by Stalder et al.²² The software uses a low-bond axisymmetric drop shape analysis (LBADSA) technique to fit the axisymmetric Young-Laplace equation to the shape of the drop. All measurements were taken three times, and reproducible to less than $\pm 3^\circ$

2.4 Results and Discussion

Morphologies of the LDPE Coatings. Initially, inverse optical microscopy was used to determine how mesh geometry and LDPE concentration affect the size and shape of the openings within the mesh. Three different stainless steel meshes (opening widths of 100 μm , 220 μm , and 1500 μm) were coated in three different concentrations of the LDPE-xylene solution (15, 30, and 60 mg/mL). As can be seen in Figure 2.1, coating thickness increased with coating concentration. The final total obscured area depended on both the initial width of the uncoated mesh, and the coating concentration. The openings within the mesh also grew more jagged and less circular as the concentration of LDPE in the coating solution increased, suggesting the formation of rougher surfaces. SEM images of the surface at multiple magnifications (Figures 2.2 and 2.3) confirm this observation.

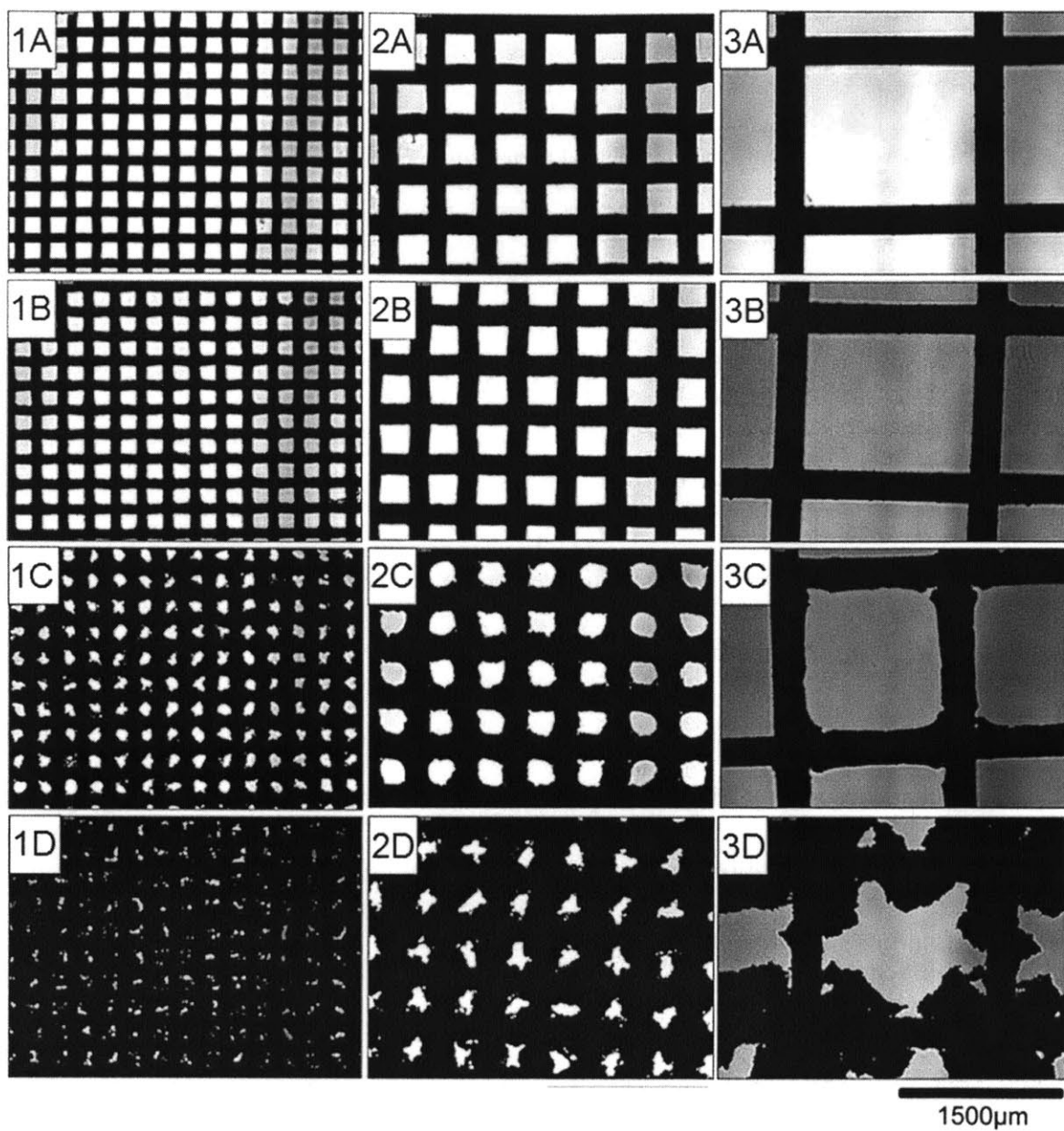


Figure 2.1: Inverse optical microscopy images of stainless steel mesh with uncoated opening widths of: (1) 100µm, (2) 220µm, and (3) 1500µm. Coating concentrations are (A) uncoated, (B) 15 mg LDPE / mL xylene; (C) 30 mg LDPE / mL xylene; (D) 60 mg LDPE / mL xylene.

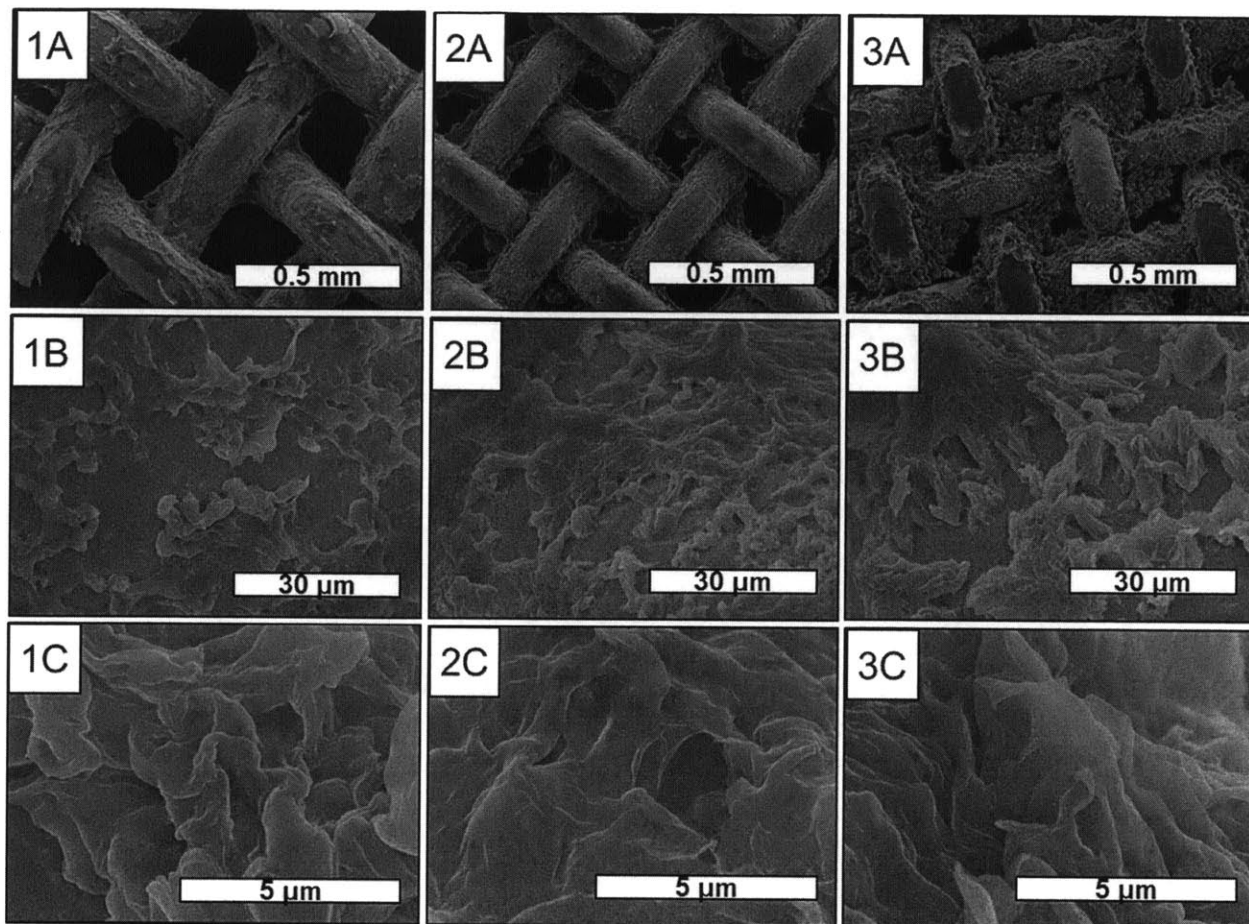


Figure 2.2: Scanning electron microscopy images of stainless steel mesh with an uncoated opening width of $220\mu\text{m}$ at varying coating concentrations and magnifications. Coating concentrations are: (1) 15 mg LDPE / mL xylene; (2) 30 mg LDPE / mL xylene; (3) 60 mg LDPE / mL xylene, and magnifications are (A) $\times 95$; (B) $\times 1600$; (C) $\times 13000$.

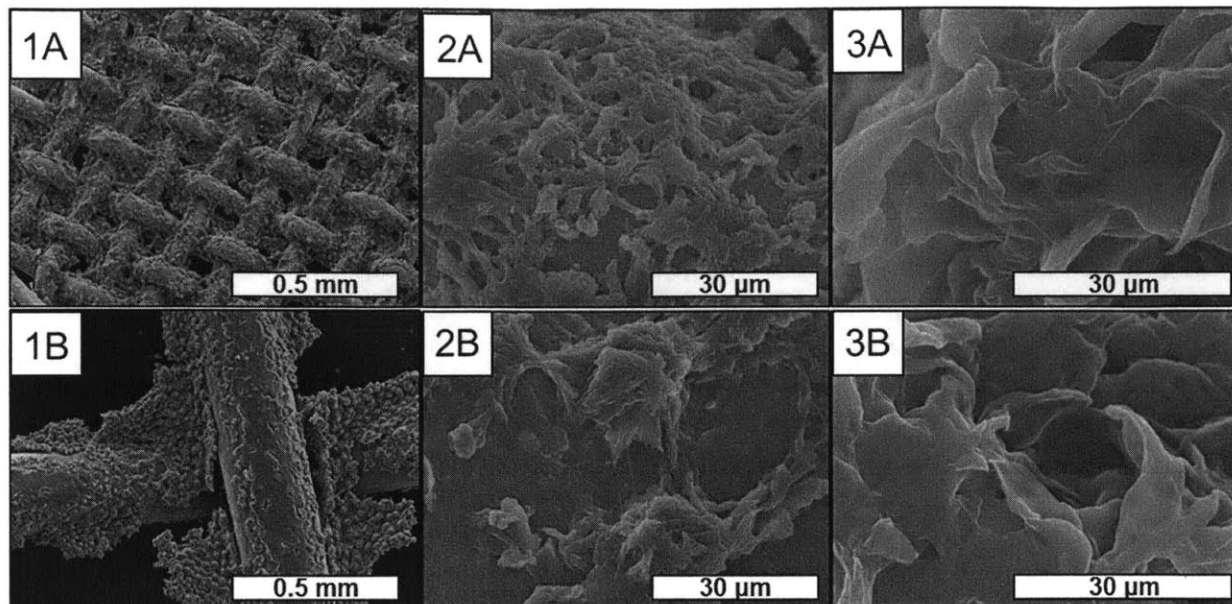


Figure 2.3: Scanning electron microscopy images of stainless steel mesh coated with a 60 mg LDPE / mL xylene solution at varying mesh sizes and magnifications. Uncoated mesh opening widths are (A) 100 μ m and (B) 1500 μ m. Magnifications are (1) x95; (2) x1600; (3) x13000.

The coating on the 220 μ m mesh (Figure 2.1 A, Figure 2.2) provides an example of the analogous pattern in surface morphology observed for all coated surfaces. Compared to the wire diameter of the bare mesh, the 15 mg \cdot mL⁻¹ LDPE-xylene solution only increased the wire diameter by about 10%. The coating tended to be flaky, and accrued in the narrower spaces within the weave. When the concentration was increased to 30mg \cdot mL⁻¹, a significant increase in the amount of LDPE coated on the mesh was observed. The SEM image indicates that the LDPE forms a thin film in the interstitial opening of the mesh, coplanar with the mesh orientation. In addition, the wires become more thickly coated with a rougher surface, again favoring the confined portions of the weave. These microstructures became even more obvious when the highest concentration of 60 mg \cdot mL⁻¹ was used (Figure 2.2 3A). The LDPE coated on the mesh

almost filled the 220 μm grid space between wires with highly irregular formations, while the most raised portions of the wires remained only lightly coated.

The same method was used to coat steel meshes with larger and smaller openings (Figure 2.1 2, Figure 2.1 3, and Figure 2.3). The 100 μm mesh had a much more complete coating, including most of the raised portions of the wires (Figure 2.3 1A). The mesh openings were nearly completely closed off, with rough, jagged edges. In contrast, the larger 1500 μm mesh had most of the LDPE concentrated in the corners or edges of the grid, creating “star-shaped” pores (Figure 2.1 3D). However, all meshes coated at this high concentration showcased similar surfaces, with microstructures particularly prominent on the interstitial LDPE. Taken all together, the LDPE coatings exhibit similar surface morphology for a given concentration, regardless of the size of the mesh opening.

Surface Roughness and Liquid Contact Angles. At the higher concentrations (30 and 60 $\text{mg}\cdot\text{mL}^{-1}$), the LDPE coated on the stainless steel mesh was visibly white in color, which is different from common, transparent solid LDPE. This could either be explained by either a highly porous LDPE coating, which would scatter light and cause the surface to appear white, or a crystalline formation of LDPE. Higher magnification SEM micrographs confirm the presence of sub-micron structures in the LDPE coating, while DSC analysis of the 220 μm mesh coated with various concentrations indicated that the coated LDPE is about 20% crystalline (Table 2.1). The masses measured were quite low, due to the low mass ratio of the LDPE coating to the steel substrate. No melting curve could be observed for the 15 mg/mL mesh due to the small sample mass. The two measured samples are mostly amorphous, with approximately

equal crystallinity. Thus, the roughness was likely caused by evaporating the xylene quickly in the well ventilated fume hood, forming amorphous LDPE with small channels for xylene evaporation. This fast evaporation created micro- and nano-structures that were visible at all concentrations.

Table 2.1: Crystallinity of LDPE coated on a 220 μm mesh.

Coating Concentration (mg/mL)	Mass of LDPE Tested (μg)	Enthalpy of Fusion (J/g)	% Crystallinity
15 ± 1	85 ± 3	BDL	N/A
30 ± 2	130 ± 4	55 ± 6	$19 \pm 2\%$
60 ± 4	344 ± 10	61 ± 7	$21 \pm 3\%$

To better quantify the roughness of the coatings on the 220 μm mesh, atomic force microscopy (AFM) was utilized to directly measure the roughness ratio (r_f in Equation 2.2). The AFM could only probe the highest, most horizontal portions of the coated meshes, since the length of the probe (7 μm) was much smaller than the inherent topography of the woven mesh, and the curvature of the wires would artificially skew the roughness ratio based on surface orientation relative to the probe. These sections tended to be free of microstructures (e.g. Figure 2.2 3A); thus, any changes would reflect the characteristics of a baseline coating. To compliment this measurement, a number distribution of pixel greyscale values was generated from the high magnification SEM images. The standard deviation of these distributions is known as the SEM index, and has been shown to correlate with surface roughness.²³ These measures of roughness are reported in Table 2.2.

Table 2.2: Roughness parameters of the 220 μm mesh with various coatings.

Coating Concentration (mg/mL)	AFM Roughness Ratio of Raised Wire Surfaces	SEM Index
Uncoated	1.005 ± 0.003	6.58
15	1.053 ± 0.003	18.6
30	1.077 ± 0.005	21.6
60	1.096 ± 0.006	24.1

Despite not being able to directly measure the roughness ratio of the thickest sections of the LDPE coating, the SEM index clearly shows an increase in surface roughness with LDPE coating concentration. The AFM results indicate that although the uppermost surfaces lack the microstructures found elsewhere, they still become rougher as the concentration of the coating solution is increased. Overall, the combination of mesh openings on the order of 100 microns, surface structures on the order of 5 microns, and sub-micron features within the microstructures suggests complex wetting behavior that can be further quantified through contact angle analysis.

While the surface chemistry of smooth LDPE alone makes it hydrophobic (water contact angle of about 100° ²⁴), a highly porous and/or rough surface will increase the local contact angle. The contact angle of a 10 μL drop of water was measured for each of the coated mesh surfaces (Figure 2.4). As expected given the existence of openings in the mesh beneath the drops (decreasing the value of f in Equation 2.2), all of the coated meshes exhibited contact angles higher than that of a smooth LDPE surface. However, the effect of increasing the coating concentration was less straightforward. The 1500 μm mesh contact angle exhibited an inverse relationship with the coating concentration, while the same relationship was non-monotonic for the 100 μm and 220 μm meshes.

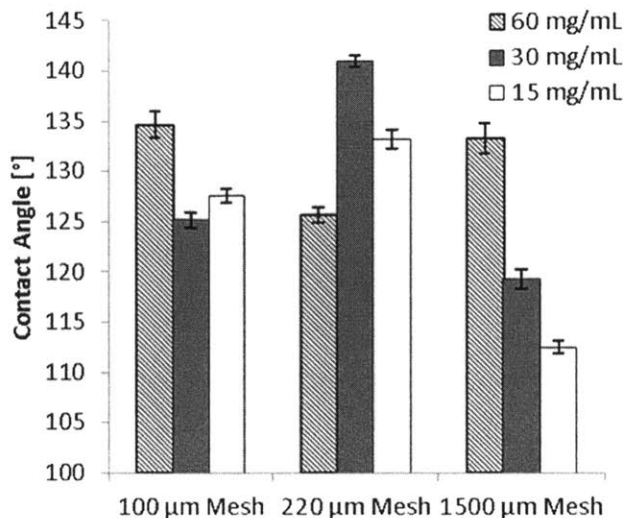


Figure 2.4: Measured water contact angles on stainless steel meshes coated in various concentrations of LDPE-xylene solutions. Mesh size refers to the width of the uncoated openings. Both the coating thickness and roughness increased with solution concentration.

The water contact angle results can be partially explained by the competing parameters f and r_f in Equation 2.2. As the concentration of the LDPE-xylene solution increased, the LDPE coating grew thicker and filled more of the area between the wires. This would increase the area fraction of the projection of LDPE in contact with the liquid (f), and decrease the apparent contact angle. However, SEM micrographs and AFM measurements revealed that higher concentrations also produced rougher coatings, which would increase the value of r_f and increase the apparent contact angle. Furthermore, increasing the roughness will increase f as well, since the submicron features on the LDPE coatings will likely not become fully wetted by the liquid. Thus, increasing the coating thickness causes both f and r_f to increase, and it is not clear which factor dominates *a priori*. For the 100 μm and 200 μm meshes, it appears that the dominating parameter switched as the coating thickened, while it is likely that the relative increase in f dominated for the largest mesh. However, without the ability to directly measure

either parameter, quantitatively decoupling these competing effects is difficult. Nevertheless, the variation in apparent contact angle and the visibly irregular microstructures strongly suggest that microscale roughness plays a significant role in determining the hydrophobic properties of these LDPE-coated meshes.

In addition to its hydrophobicity, we observed that the LDPE-coated stainless steel mesh was oleophilic, with apparent contact angles for the canola, olive, castor, and crude oils of about 0° . We also observed that the LDPE coated mesh has contact angle of 0° for ethanol and dichloromethane. After rinsing with dichloromethane, SEM micrographs revealed no deterioration of the coating or microstructures (Figure 2.5), demonstrating that the coated mesh can be cleaned with monopolar organic solvents and reused.

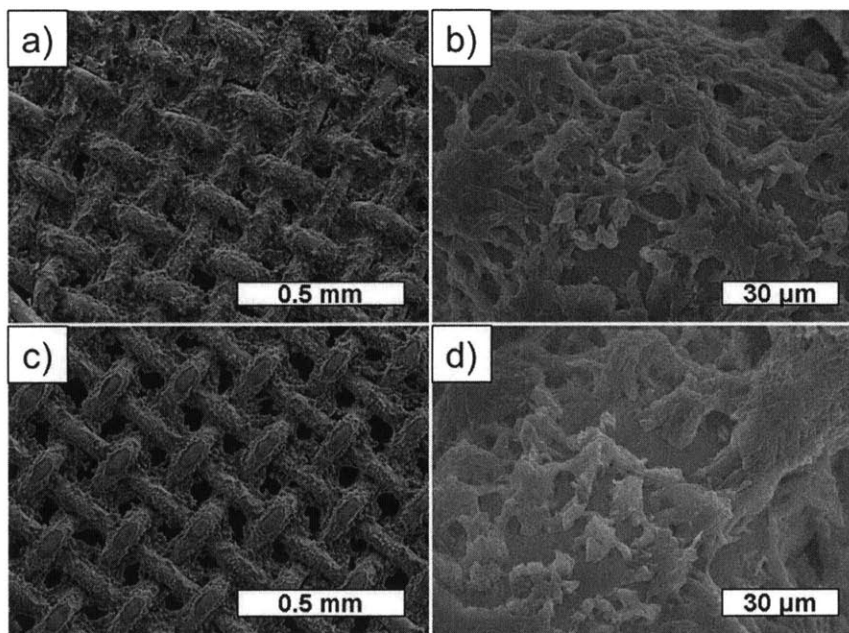


Figure 2.5. SEM images of a 100 μm mesh with a 60 mg/mL LDPE-xylene coating before (a, b) and after (c, d) separating crude oil and rinsing with dichloromethane.

After the oil contact angle experiments, it was observed that the area of mesh which came in contact with the oil was slightly darker in color than other portions. This discoloration indicates persistent wetting by the oil, which was confirmed with SEM micrographs (Figure 2.6). The water contact angle for the 100 μm mesh with a 60 $\text{mg}\cdot\text{mL}^{-1}$ coating wetted with olive oil decreased from $127\pm 2^\circ$ to $108\pm 2^\circ$. The oil displaced any trapped air associated with the rough LDPE surface, and consequently attenuated the roughness effect. That is, the wetted surface became a composite interface of oil and LDPE, not air and LDPE as assumed in Equation 2.2. Due to the relatively similar intermolecular forces of LDPE and the experimental oils, the wetted mesh behaved more like a homogeneous LDPE surface than a composite surface. Future separation applications of rough surfaces in the presence of a wetting fluid should account for the attenuation of the roughness effect with respect to water breakthrough pressure.

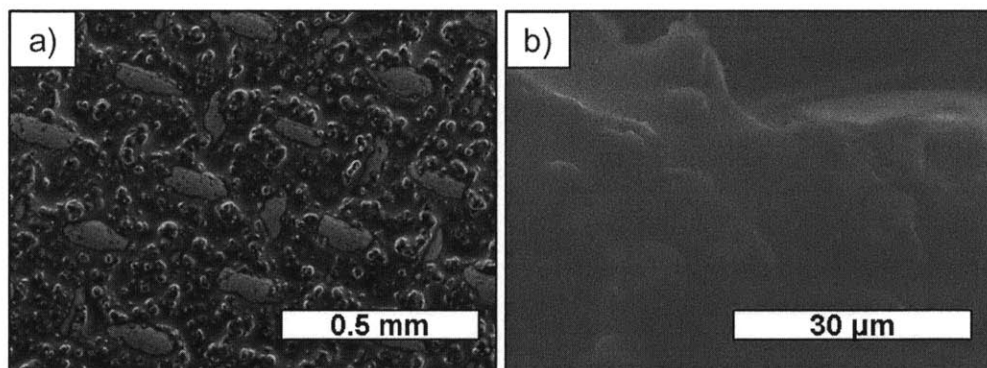


Figure 2.6: Olive oil wetting a 100 μm mesh coated with a 60 mg/mL LDPE-xylene solution. The oil fills the interstitial spaces of the mesh (a), making the surface much smoother (b).

2.5 Conclusions

Creating a hydrophobic surface on a steel mesh using an LDPE-xylene solution appears to be a feasible approach to separating oil and water. The coating method creates roughness on multiple scales, and adheres to the metallic substrate strongly enough to resist dissolution by dichloromethane. This method is particularly advantageous because the coating thickness and roughness is consistent and can be easily controlled, providing a tunable system to test the relationship between surface characteristics, mesh geometry, and separation performance.

One possible downside is the inability to measure the contact angles in a way that meaningfully corresponds to parameters specified in wetting theory. Simple wetting theory was unable to fully capture the complex wetting behavior due to the complex nature of the coated mesh surface. The inherent roughness provided by the woven wires prevented direct measurement of the roughness of the coated wire surface with AFM. This made it impossible to disentangle the effects of surface roughness and fractional contact area (which is not the same as the area obscured by LDPE). However, this incomplete characterization may not be necessary: the roughness effects are likely attenuated by persistent wetting of oil. During or after oil separation, the coating will behave more like a smooth LDPE surface. Thus, the many attempts in the literature to create a selectively wetting surface that is “superhydrophobic” may be misguided for the purposes of separation. Efforts to improve characteristics like water breakthrough pressure should focus on other mechanisms.

2.6 References

- (1) Feng, L.; Zhang, Z.; Mai, Z.; Ma, Y.; Liu, B.; Jiang, L.; Zhu, D. *Angew. Chem., Int. Ed.* **2004**, *43*, 2012-2014.
- (2) Tu, C.; Tsai, C.; Wang, C.; Kuo, S.; Chang, F. *Macromol. Rapid Commun.* **2007**, *28*, 2262-2266.
- (3) Wu, J.; Chen, J.; Qasim, K.; Xia, J.; Lei, W.; Wang, B. *J. Chem. Technol. Biotechnol.* **2012**, *87*, 427-430.
- (4) Lee, C.; Baik, S. *Carbon* **2010**, *48*, 2192-2197.
- (5) Lee, C.; Johnson, N.; Drelich, J.; Yap, Y. K. *Carbon* **2011**, *49*, 669-676.
- (6) Li, M.; Xu, J., Lu, Q. *J. Mater. Chem.* **2007**, *17*, 4772-4776.
- (7) Wang, C.; Yao, T.; Wu, J.; Ma, C.; Fan, Z.; Wang, Z.; Cheng, Y.; Lin, Q.; Yang, B. *ACS Appl. Mater. Interfaces* **2009**, *11*, 2613-2617.
- (8) Pan, Q.; Wang, M.; Wang, H. *Appl. Surf. Sci.* **2008**, *254*, 6002-6006.
- (9) Wang, S.; Song, Y.; Jiang, L. *Nanotechnology* **2007**, *18*, 015103.
- (10) Xue, Z.; Wang, S.; Lin, L.; Chen, L.; Liu, M.; Feng, L.; Jiang, L. *Adv. Mater.* **2011**, *23*, 4270-4273.
- (11) Howarter, J. A.; Youngblood, J. P. *J. Colloid Interface Sci.* **2009**, *329*, 127-132
- (12) Yang, J.; Zhang, Z.; Xu, X.; Zhu, X.; Men, X.; Zhou, X. *J. Mater. Chem.* **2012**, *22*, 2834-2837.
- (13) Yuan, J.; Liu, X.; Akbulut, O.; Hu, J.; Suib, S. L.; Kong, J.; Stellacci, F. *Nat. Nanotechnol.* **2008**, *3*, 332-336.
- (14) Liu, K.; Jiang, L. *Nanoscale* **2011**, *3*, 825-838.
- (15) Deng, D.; Prendergast, D.P.; MacFarlane, J.; Bagatin, R.; Stellacci, F.; Gschwend, P.M. *ACS Appl. Mater. Interfaces* **2013**, *5*(3), 74-781.
- (16) Young, T. *Philos. Trans. R. Soc. London* **1805**, *95*, 65.
- (17) White, I.; Sully, M.J. *Water Resour. Res.* **2010**, *23*(8), 1514-1522.
- (18) Cassie, A. B. D.; Baxter, S. *Trans. Faraday Soc.* **1944**, *40*, 546-551.

- (19) Quéré, D; *Physica A* **2002**, 313, 32-46.
- (20) Yao, X.; Song, Y.; Jiang, L. *Adv. Mater.* **2011**, 23(6), 719-734.
- (21) Wunderlich, B; *Thermal Analysis*, 1st ed.; Academic Press: New York, 1990; p 780.
- (22) Stalder, A.F.; Melchior, T.; Müller, M.; Sage, D.; Blu, T.; Unser, M. *Colloids Surf., A* **2010**, 364, 72-81.
- (23) Banerjee, S.; Yang, R.; Courchene, C. E. *Ind. Eng. Chem. Res.* **2009**, 48, 4322-4325.
- (24) Lu, X.; Zhang, C.; Han, Y. *Macromol. Rapid Commun.* **2004**, 25, 1606-1610.

Chapter 3 – Water Breakthrough Pressure

3.1 Introduction

The ability of the hydrophobic mesh to repel water is a key performance metric. Minimizing the amount of water recovered with spilled oil improves collection rates and reduces the treatment costs associated with dewatering the oil. Water breakthrough occurs when free phase water passes through the mesh, contaminating the oil permeate. This is a serious failure mechanism, since water percolation is difficult to stop once started. When the hydrostatic water pressure becomes high enough to overcome the repulsive capillary pressure within the mesh openings, water begins to flow and does not stop until the hydrostatic pressure is reduced by a significant amount.¹ This capillary pressure depends on both the size of the mesh pores, and the material of the mesh surface. Simple sessile droplet tests of hydrophobicity do not guarantee high breakthrough resistance. While a hydrophobic mesh easily prevents the permeation of a water droplet, resisting the breakthrough of a water column is much more difficult.

In the literature, the breakthrough pressure of a non-wetting liquid through a selectively wetting mesh is much less commonly reported than other factors, such as the non-wetting contact angle and separation efficiency. Jian et al.² used the basic capillary height equation (see Section 3.2) to try and predict the intrusion pressure of water through a copper mesh coated with a fluoropolymer. Their predictions were consistently lower than the observed heights by

about 20-40%. A similar result occurred in the work of Tian et al.,³ who found that the same expression underpredicted the intrusion of water through a ZnO coated steel mesh.

On the other hand, Xue et al.⁴ created a steel mesh with a hydrophilic/oleophobic coating of polymerized hydrogel and found that the capillary height equation correctly predicted the intrusion pressure of various oils. Unfortunately, this intrusion pressure was very low, and the large uncertainties from experimental measurement may have masked any systematic deviation from theory. The purpose of this section is to more thoroughly explore the relationship between mesh characteristics (geometry and surface properties) and the breakthrough pressure of water, in order to develop a predictive expression.

3.2 Theory

Deploying hydrophobic mesh as an oil spill remediation device will involve partially submerging the mesh under water when oil is not present. This demand requires knowledge of the hydrostatic pressure that will cause undesired water to be forced through the hydrophobic mesh. The classical Young-Laplace equation^{5,6} describes the static pressure difference across the water-air meniscus that forms within each capillary-like opening in the coated mesh

$$\Delta P = \gamma_{LG} \left(\frac{1}{R_1} + \frac{1}{R_2} \right) \quad (3.1)$$

where γ_{LG} is the air-water surface tension, and R_1 and R_2 are the two orthogonal radii of curvature of the interface. Water will break through the mesh when the local water pressure

becomes greater in magnitude than the capillary pressure within the mesh openings. Balancing these pressures gives the capillary height equation,⁶

$$h = \frac{2\gamma_{LG} \cos \theta}{\rho g r} \quad (3.2)$$

where h is the water depth, ρ is the density of water, g is the gravitational acceleration, r is the radius of the opening, and θ is the contact angle between the liquid and the solid. This basic theory predicts that the breakthrough height of water is inversely proportional to pore size, and will increase for more hydrophobic surfaces.

For a non-wetting fluid, the capillary height equation only applies when the opening is perfectly circular and roughly two-dimensional. However, due to the shape of the wire weave, the surface of the coated mesh has a significant variation in height compared to the depth of the pores (e.g. Figure 2.2). In order to better apply Equation 3.1, the mesh openings were idealized to be similar to the hole of a torus. This idealization is an attempt to capture the effect of both the geometry of the woven steel wires, and the shape of the opening after an LDPE coating is applied. The cross-section of such a shape is shown in Figure 3.1. As an additional simplification, the meniscus is assumed to take the shape of an axisymmetric spherical cap, which reduces the two orthogonal radii of curvature to a single, mean radius of curvature. The meniscus, oriented to oppose the hydrostatic pressure of the water, must maintain a constant contact angle relative to the tangent of the surface as determined by Equation 2.2.

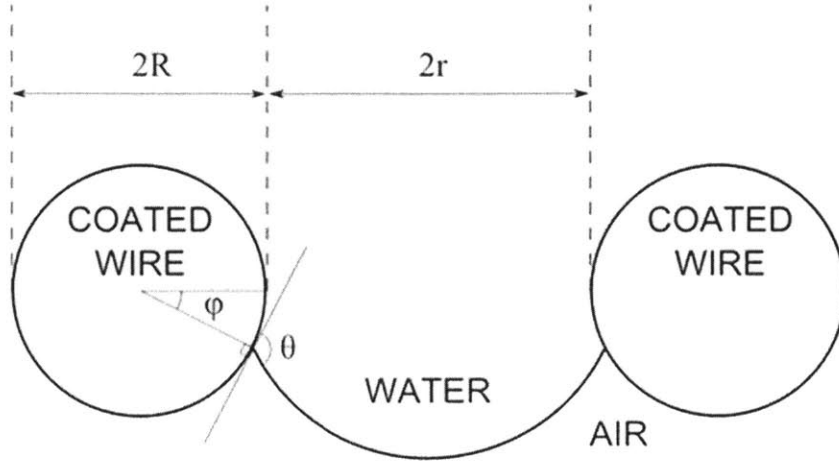


Figure 3.1: Cross-section of the water meniscus suspended within an idealized coated mesh opening. As the water column height above the meniscus changes, the contact point (located by the angle from the horizontal φ) moves up or down the surface of the wire, while maintaining a constant contact angle θ relative to the local tangent.

Liu and Lange⁷ used a similar approach to describe the pressure required to transition to a fully wetted state from a Cassie-Baxter state on a flat surface with a regular array of spherical protrusions. Most importantly, their model incorporated an unpinned interface, which shifted its position in order to match the applied pressure while maintaining a constant local contact angle as determined by Equation 2.2. By adapting their capillary pressure equation for our proposed model, and setting the pressure equal to the hydrostatic pressure of water, the depth of water h required to break through the LDPE-coated mesh was estimated to be

$$h = \frac{2\gamma_{LG} \cos(\theta + \varphi)}{\rho g (r + R[1 - \cos \varphi])} \quad (3.3)$$

where r is the radius of mesh opening, R is the radius of the coated wire, and φ is the angle the contact point makes with the horizontal. When φ is equal to zero, Equation 3.3 is reduced to

Equation 3.2. As the contact line moves down the pore, the term $R[1 - \cos \varphi]$ captures the widening of the pore, while the term $\cos(\theta + \varphi)$ represents the apparent contact angle of the meniscus, as seen relative to the vertical in Figure 3.1. Since these two factors are in the denominator and numerator, respectively, they compete against one another as φ increases from zero to $\pi - \theta$. Thus, Equation 3.3 has some maximum value of h as a function of φ , which represents the maximum depth a mesh with given values of r , R , and φ can withstand before water intrusion occurs.

Strictly speaking, the local contact angle θ must take into account local roughness and fractional wetted area, neither of which are known. The model assumes the local contact angle is equal to that of a smooth LDPE surface. The maximum height is relatively insensitive to θ compared to r and R , especially given the large variance in pore dimensions (see Table A.1). As an example, for the 220 μm mesh with a 60 $\text{mg}\cdot\text{mL}^{-1}$ coating, it would take a local contact angle of 143° to match the error introduced by the moderate variance in the pore radius. This assumption allows us to find the mean radius of curvature using the radius of the mesh opening and the contact angle between water and the LDPE surface.

3.3 Methods

Materials. All meshes were fabricated as described in Section 2.3.

Water Breakthrough Pressure. The depth at which the hydrostatic water pressure overcomes the capillary pressure within the mesh openings is the maximum operation depth for a given mesh. To test this, a sample of multiple mesh sizes were coated in various

concentrations of an LDPE-xylene solution as described above. Then, each mesh was affixed to the end of a glass tube using clamps and PTFE O-rings. Water was slowly added to the glass tube, increasing the height of water, until water breakthrough was observed (typically a small leak). To avoid disturbing the air-water interface within the mesh, the water was added slowly via a thin tube. Care was also taken to ensure percolation did not occur around the edges of the O-rings.

Characterization of Mesh Geometry Using Optical Microscopy. Physical dimensions of the coated and uncoated meshes were measured using an inverted optical microscope (TE2000; Nikon). Due to irregularities in pore size and shape, the average dimensions were found statistically. First, the areas of a large sampling of openings for each mesh/coating combination were measured and the mean opening area was determined. Then, this mean area was used to calculate an effective pore radius r of a circle with equivalent area. The corresponding effective coated wire radius R was calculated by halving the width of an uncoated mesh opening, subtracting the effective pore radius, and adding the radius of the uncoated wire. An exception was made for meshes coated with a $15 \text{ mg}\cdot\text{mL}^{-1}$ LDPE-xylene solution, since using this method would result in an effective coated wire radius smaller than the radius of an uncoated wire. In that case, the coated wire radius R was measured directly. A summary of these coated-mesh properties can be found in Appendix Tables A.1 and A.2.

3.4 Results and Discussion

Initially, we assumed that the simple capillary height equation would be sufficient to predict the breakthrough depth of water, following the trend used in the literature. The $100 \text{ }\mu\text{m}$,

220 μm , and 1500 μm meshes were coated with concentrations of 60 $\text{mg}\cdot\text{mL}^{-1}$. Optical microscopy was used to find the mean effective pore radius and coating radius. Figure 3.2 compares the height predicted by the capillary height equation (Equation 3.2) and the one derived from Liu and Lange (Equation 3.3) to the observed height of the water column above the mesh.

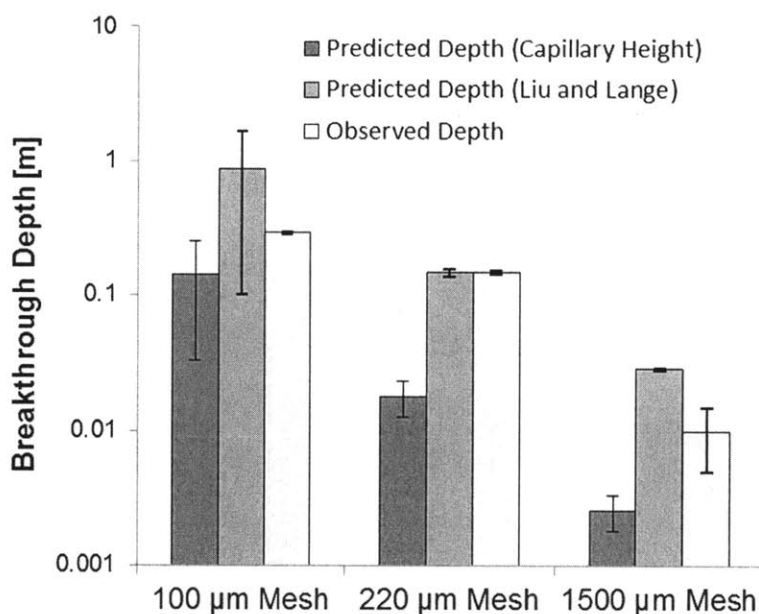


Figure 3.2: Comparison of the observed breakthrough heights and those predicted by two models: the classic capillary height equation and one modified from Liu and Lange⁷. Error bars represent experimental precision for the observed values, and propagation of variance from average pore size calculations for the predictions.

In these preliminary experiments, the two models performed very differently. The capillary height equation consistently under-predicted the breakthrough depth of the water column, with the error bars overlapping only on the mesh with the smallest openings, which had the largest propagated error. Moreover, this error cannot be attributable to a poorly known local contact angle: given all other variables, the capillary height equation predicts that the observed heights for the 220 μm and 1500 μm meshes would be impossible to achieve for any

local contact angle. Error resulting from other variables is unlikely, as these are well defined physical constants.

However, the model developed from the work of Liu and Lange is a superior predictor of breakthrough depth. The observed depths matched the predictions to within quantifiable uncertainty, excluding the largest mesh. For that particular case, the discrepancy can be attributed to the large, non-circular pore openings (Figure 2.1 3D), which would support a highly non-ideal meniscus. Given such large and irregular morphology, Equation 3.3 will be a poor predictor of the breakthrough depth. To test this formulation more rigorously, the breakthrough depths of additional meshes was tested using an identical method (Figure 3.4). The decision to test the range of meshes chosen was based on practical operational depths: all have a predicted breakthrough depth of at least 5 cm.

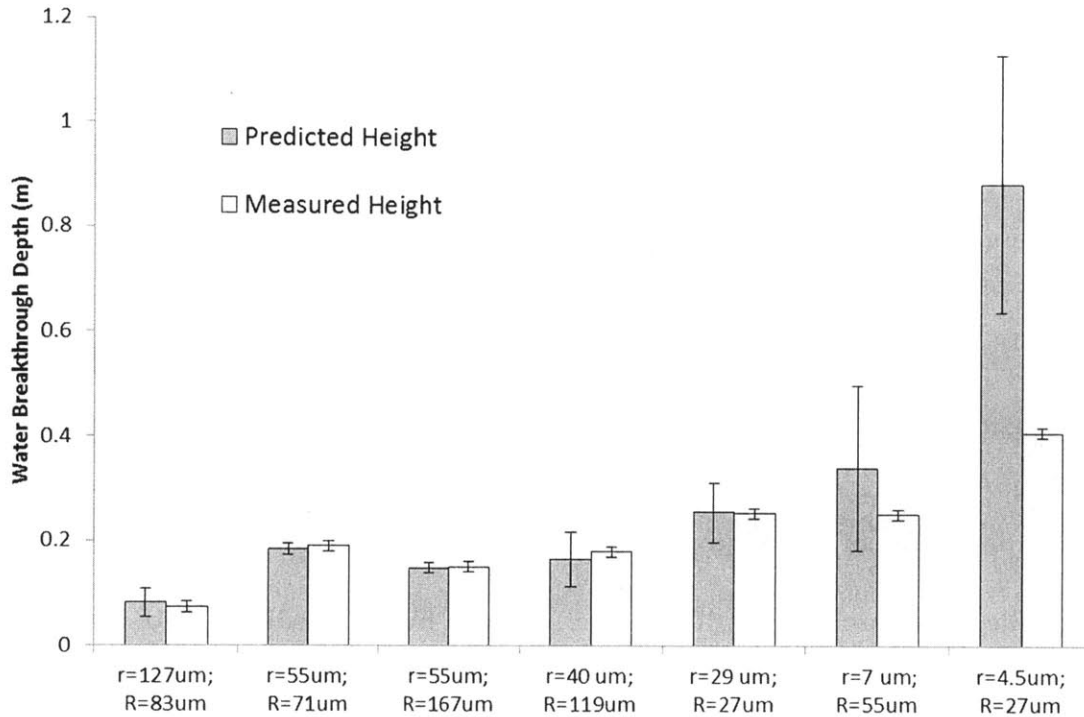


Figure 3.3: Breakthrough depths of various mesh geometries. Predicted height is based on a model derived from Liu and Lange⁷. Error bars represent experimental precision for the observed values, and propagation of variance from average pore size calculations for the prediction.

Again, the predictive model matched the observed breakthrough depth for all but one of the tested mesh geometries. More importantly, the data clearly shows the dependence of breakthrough depth on the coated wire radius R . The meshes portrayed by the 2nd and 3rd columns of Figure 3.3 differ only in the coated wire radius. Without changing the mean pore radius, the observed height increased from 15 ± 1 cm to 19 ± 1 cm. In addition, when the mean pore radius was decreased from 29 ± 6 μ m to 7 ± 4 μ m, but the coated wire radius increased from 27 ± 15 μ m to 55 ± 5 μ m (Figure 3.3, 5th and 6th columns), the observed breakthrough height remained unchanged. In this case, the increase in breakthrough depth from decreasing the

mean pore radius was balanced by the increase in the coated wire radius. Such behavior is not accounted for in the capillary height equation, but here is predicted by Equation 2.3. This model only failed for the coated mesh with the smallest opening. This could be due to insufficient sampling of pore sizes, or the highly jagged, non-circular openings (Figure 2.2 3A). However, the expression serves as a surprisingly good predictor in the other cases, given the heterogeneity seen in the pore size distribution and morphology.

3.5 Conclusions

The development of an unpinned meniscus model in this work proved critical to predicting the breakthrough depth of water. Simple theory predicted two possible design variables: the local contact angle and the pore radius. However, such idealized theory was unable to explain the large depths achieved by these hydrophobic meshes. By taking the theory a small step further by incorporating local geometry and an unpinned interface, we were able to successfully predict the breakthrough depths for meshes with pore sizes in the range of 7 – 220 μm , corresponding to depths of about 5 – 40 cm.

The form of the model equation also provides further evidence that the breakthrough pressure does not depend heavily on surface properties. The insensitivity of Equation 3.3 to θ appears to be caused by the mobile meniscus moving further into the mesh opening (higher φ) under increased pressure. This repositioning allows it to increase the interfacial pressure, but negates much of the effect caused by a larger local contact angle. Thus, material substitutions such as PTFE for LDPE (flat water contact angles of 110° ⁸ and 100° , respectively) will have little impact on breakthrough resistance. In addition, as discussed in Section 2.5, persistent wetting

by separated oil will attenuate any roughness effects, creating an apparently smooth surface. Therefore, the most important factor for improving the breakthrough resistance of hydrophobic meshes is the geometry of the mesh weave, incorporating both the size of the opening and the diameter of the coated wires.

These results also provide an interesting insight for design purposes. The demonstrated influence of the coated wire radius R provides another variable that can be tuned to achieve desired performance goals. Under simple theory, this design parameter would not have been noticed without empirical testing. By incorporating a small addition to an idealized model, we were able to account for unexpected results, and develop a predictive formulation for breakthrough depths relevant to implementation. This algorithm will be a necessary portion of the overall optimization of hydrophobic meshes for oil spill recovery.

3.6 References

- (1) Noblin, X.; Buguin, A.; Brochard-Wyart, F. *Eur. Phys. J. E* **2004**, *14*, 395-404.
- (2) Jiang, Z.X.; Geng, L.; Huang, Y.D. *J. Phys. Chem.* **2010**, *114*, 9370-9378.
- (3) Tian, D.; Zhang, X.; Wang, X.; Jin, Z.; Jiang, L. *Phys. Chem. Chem. Phys.* **2011**, *13*, 14606-14610.
- (4) Xue, Z.; Wang, S.; Lin, L.; Chen, L.; Liu, M.; Feng, L.; Jiang, L. *Adv. Mater.* **2011**, *23*, 4270-4273.
- (5) Young, T. *Philos. Trans. R. Soc. London* **1805**, *95*, 65.
- (6) Laplace, P.S. *Traite de Mechanique Celeste*; Gauthier-Villars, Paris, 1805; Vol. 4, Supplements au Livre X.
- (7) Liu, B.; Lange, F.F.; *J. Colloid Interface Sci.* **2006**, *298*, 899-909.
- (8) Veeramasuneni, S.; Drelich, J.; Miller, J.D.; Yanauchi, G.; *Prog. Org. Coat.* **1997**, *31*, 265.

Chapter 4 – Oil Permeate Flux

4.1 Introduction

In addition to preventing water from breaking through, the hydrophobic mesh should maximize the rate at which oil passes through. Much of the previous work with selectively wetting meshes has devoted little effort into understanding the flux through the meshes. In the rare instances when permeate flux is reported, the hydrodynamic conditions are unclear or unable to be extrapolated. Examples include: reporting the time required for a single droplet to fall through the mesh,^{1,2,3} reporting a time averaged flow value while varying the hydrostatic head to an unknown extent,^{4,5} or using the mesh in a cross-flow orientation.⁶ This reporting of flow values under different hydrodynamic regimes complicates comparison, making oil flux the most poorly understood parameter relevant to mesh performance. In general, flux values of all oil-water separation filters tend to be in the range of 0.05 to 5 L·m⁻²·s⁻¹, with the higher values consistently assigned to separations driven by hydrostatic pressure.^{3,4,5}

Herein, a bench-scale recovery device incorporating the hydrophobic mesh is described and used to recover floating oil from a small container of water. Since testing is done under stationary conditions, and most unconfined oil spills are less than 1 mm thick,⁷ capillary action will be the dominant driver of flow. This phenomenon is identical to the one preventing water from intruding, but works in reverse for wetting liquids. Floating oil is brought into contact with the exterior of the mesh and wets it. Capillary action then “pulls” the oil through the small openings of the oleophilic mesh, which continues to flow out the other side. Applying Equation

3.2 to oil ($\rho \cong 900 \text{ kg}\cdot\text{m}^{-3}$, $\gamma_{LG} \cong 0.03 \text{ N}\cdot\text{m}^{-1}$, $r \cong 10^{-4}\text{m}$, $\theta = 0^\circ$) indicates that the oil must be at least 6 cm thick to provide an equal pressure from hydrostatic head. Thus, flow due to hydrostatic head can be negated.

This section also determines the separation efficiency of the mesh. This value is much more commonly reported in the literature, and is important in predicting permeate feed contamination and determining whether water is drawn into the pores by viscous effects from the oil.

4.2 Theory

The most relevant transport mechanism for flow through the LDPE-coated mesh is capillary action. Assuming that each mesh opening acts like an individual capillary pore, the Washburn equation⁸ can be applied to estimate the flow rate

$$v = \frac{\gamma_{LG}r}{4\eta(2R)} \quad (4.1)$$

where v is linear velocity of oil moving through a mesh pore, γ_{LG} is the liquid-gas surface tension of the oil, η is the dynamic viscosity of the oil, r is the radius of the pore, and R is the coated wire radius. The Washburn equation is derived from Poiseuille's law, and assumes that the hydrostatic head of the oil is neglected, the oil fully wets the LDPE coating, and the capillary length is approximated to be twice the coated wire radius ($2R$). To convert this expression into volumetric flux q for the entire mesh, the velocity is multiplied by the area of the pore πr^2 and the inverse of the area occupied per pore $1/(2r + 2R)^2$

$$q = \frac{1}{4(r + R)^2} \cdot \frac{\pi\gamma_{LG}r^3}{4\eta(2R)} \quad (4.2)$$

With regard to oil characteristics, the flux through the mesh will be directly proportional to the surface tension of the oil, and inversely proportional to the viscosity. Oil surface tension values tend to vary little across many oils.⁹ However, viscosity can vary by many orders of magnitude, depending on both oil composition and temperature.⁹

Regarding characteristics of the mesh, the oil permeate flux is directly proportional to the radius of the mesh openings. This relationship is in opposition to that between pore radius and breakthrough pressure (Section 3.5), suggesting a possible trade-off between these two performance parameters. On the other hand, Equation 4.2 suggests that the oil flux is very sensitive to the coated wire radius ($q \propto R^{-3}$), while breakthrough depth h is significantly less so (Equation 3.3, $h \propto R^{-1}$ approximately). Thus, this chapter will focus on determining the influence of oil viscosity, mesh pore radius, and mesh coated wire radius on the oil permeate flux.

4.3 Methods

Materials. All materials were used as received. Meshes were fabricated as described in Section 2.3. Southern Louisiana crude oil was obtained from John Farrington of the Woods Hole Oceanographic Institute, while the other oils (castor, olive, and canola) were obtained from grocery stores. This set of oils reflects a broad range of viscosities encompassing those found for many crude oils (Table 1). The oil viscosities were measured using a bubble time method in accordance with ASTM D-1545, and the surface tensions were measured using the

capillary rise technique. Seawater was collected from the Port of Christopher Columbus Waterfront Park in Boston, MA.

Table 4.1: Physical properties of oils tested with oil-water separation device.

Sample	Surface Tension^a (dyne/cm)	Viscosity^a (cP)
Canola Oil	30.9 ± 0.7	73 ± 9
Olive Oil	30.2 ± 0.9	75 ± 9
Castor Oil	31.0 ± 0.7	780 ± 13
Southern Louisiana Crude Oil	28.8 ± 0.6	64 ± 9

^a Measured at the experimental temperatures: 23±1°C

Oil Spill Recovery. Experimental testing was performed in order to quantitatively assess the ability of the mesh to continuously recover four different types of oils (canola, olive, castor and Southern Louisiana crude oil) from atop a pool of water. Two experimental setups were utilized. The initial apparatus consisted of coated mesh mounted on the sides of a glass test tube (1" OD) so as to cover "windows" cut in the side of the tube. The test tube was then immersed in a beaker with 400 mL of distilled water beneath a 25 mL layer of oil (0.5 cm thick) such that the mesh window was in contact with the oil layer (Figure 4.1). The oil immediately flowed through the mesh windows and pooled at the bottom of the test tube from which it was continuously pumped and collected in a separate graduated cylinder. The recovered volume was recorded as a function of time.

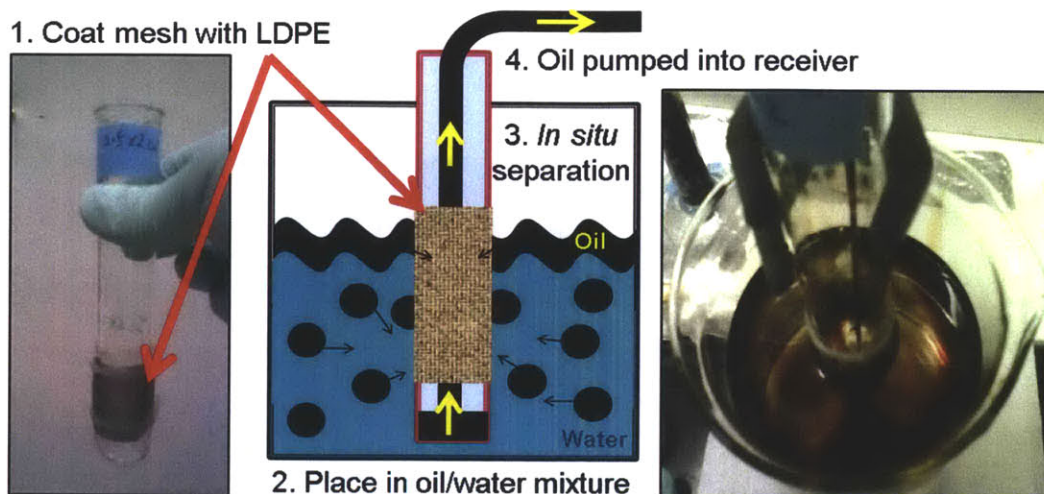


Figure 4.1: Photos and diagram of initial recovery apparatus. Center: illustration showing the integrated collection system recovering oil; blue represents seawater, black represents a crude oil spill. Left: photo of the test tube with windows cut in its side covered with a LDPE-coated mesh. This tube was lowered into beakers with floating oil. The oil passed through the mesh and was continuously pumped to an external reservoir. Right: photo showing the system during operation. Oil removal occurred on the sides of the device with mesh (left and right in the photo), but not elsewhere (e.g., bottom of photo).

A second experimental apparatus was developed to better measure the oil flux through the mesh. Observed flow rates in the initial setup were limited by the spreading of oil across the water surface, not capillary action through the mesh. This limitation is apparent in the rightmost photo of Figure 4.1, which shows the uneven layer of oil after only 30 seconds. To overcome this limitation, the second apparatus was designed to return the recovered oil to the pool of oil, directly in front of the mesh (Figure 4.2). A single mesh was clamped to a glass tube and sealed with PTFE O-rings. Oil permeate could be collected in a small pool below the mesh, but was immediately returned to the surface using a peristaltic pump. Flow rate was measured after the system reached steady-state by rerouting the return line to a graduated cylinder for 10 seconds. Experiments were repeated in triplicate.

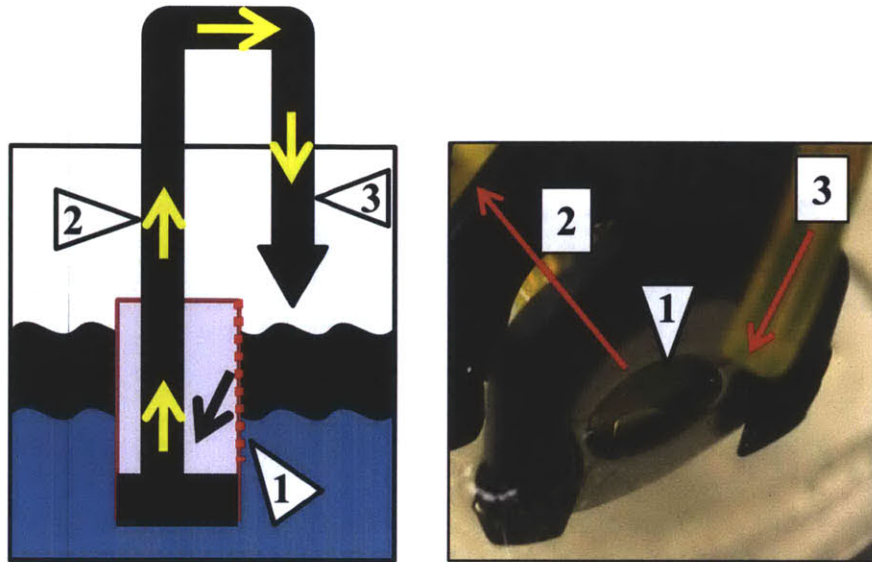


Figure 4.2: Steady-state apparatus design, with return flow to ensure a constant supply of oil in the beaker. Left: Diagram of the apparatus, where blue is water and black is oil. Right: Photo of the mesh incorporated into the apparatus. The olive oil is yellow, and both can be seen in contact with the mesh surface. Process: (1) Mesh separates the oil and water; (2) Oil permeate is collected and removed from the recover device (3) Oil permeate is returned to the floating oil.

The first series of recovery experiments used the same 220 μm swatch of mesh coated in 60 $\text{mg}\cdot\text{mL}^{-1}$ solution of LDPE-xylene while varying the oil. The mesh was rinsed with dichloromethane and air-dried between experiments. The second series of experiments used seawater and a single oil, olive, while varying the coated mesh pore size and wire radius (mesh coating details can be found in Appendix Table A.2).

Determination of the Permeate Water Content. After each oil recovery experiment, an aliquot of oil permeate was immediately collected, sealed within a pre-weighed wide glass vial, and weighed again. The vial was later opened, sealed within a larger jar containing anhydrous calcium sulfate, and kept at 60 $^{\circ}\text{C}$ for no less than 3 h. After cooling, the water content was

determined gravimetrically from both the mass lost by the sample, and the mass gained by the desiccant. The detection limit for this method was determined to be 1% water by mass, based on error using external standards and agreement between the two mass differences.

4.4 Results and Discussion

Initial experiments with the apparatus described in Figure 4.1 had a significant limitation. While oil initially flowed through the mesh at a rapid rate, the flow would taper off over time. This limitation was due to reducing the finite volume of oil, which adhered to the walls of the beaker while spreading thinly near the mesh (see rightmost photo in Figure 4.1.) Thus, only the initial flow rate represented the mesh's capability. At longer times, flow was dictated by the rate at which the oil could spread across the surface of the water.

Although this hampered the ability of the apparatus to accurately measure oil permeate flux, it did provide evidence that the mesh could pass oil more rapidly than it could spread on the surface. This initial setup was used for all four oils, on both deionized and seawater. Because the Southern Louisiana crude oil is considered to be "light" crude, it tends to spread faster over water than other, more viscous oils.⁷ Therefore, hydrophobic meshes will, at the very least, recover oil at a sufficient rate to be implemented as a stationary device in stagnant waters.

However, in order to fully assess the potential recovery rate *via* capillary action, the experimental setup was redesigned to provide a constant supply of oil (Figure 4.2). This apparatus ensured a steady flow of oil was passing through the mesh before a flow rate

measurement was taken. Figure 4.3 shows the result of varying the pore radius and coated wire radius.

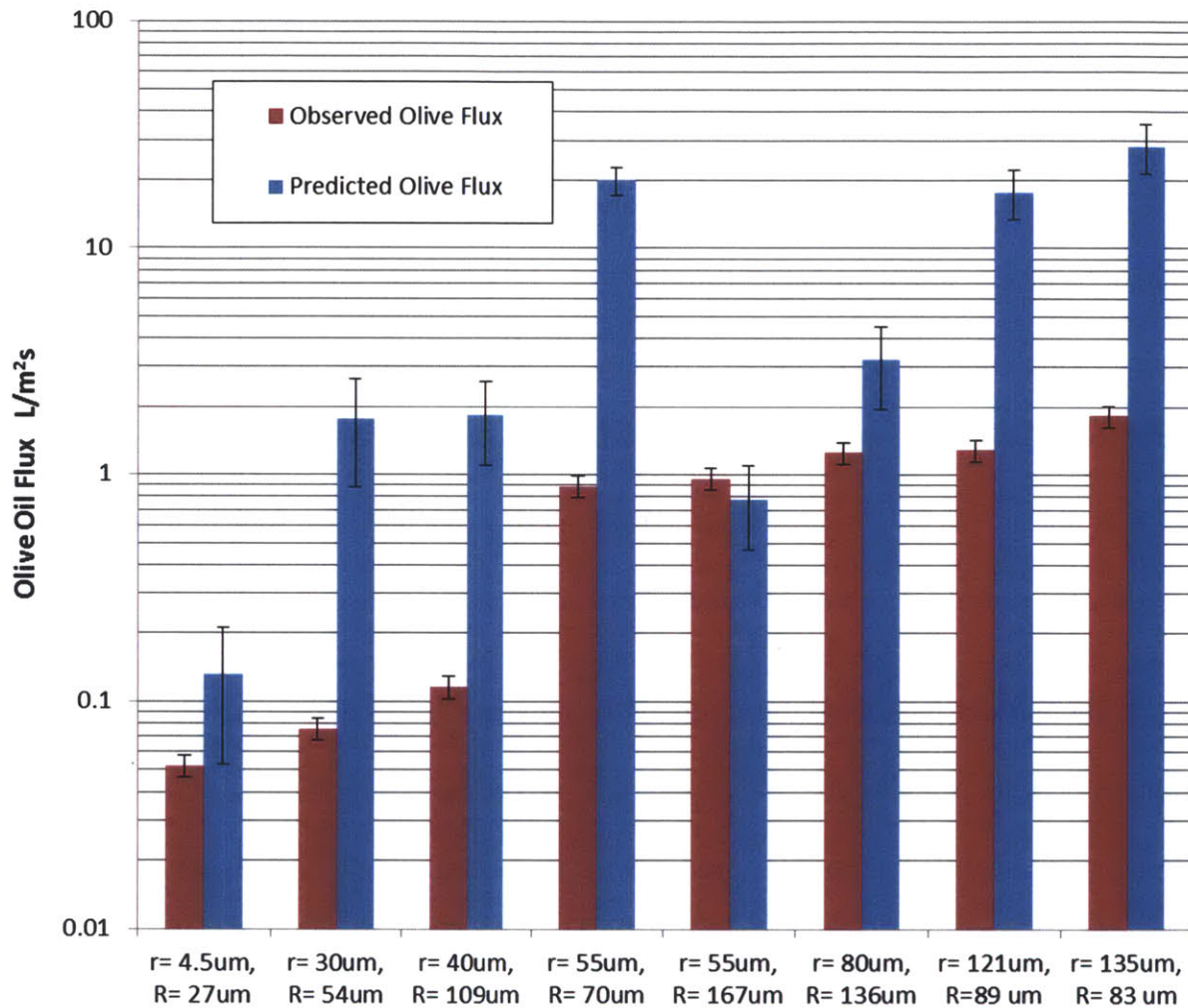


Figure 4.3: Comparison of predicted and observed olive oil permeate flux through hydrophobic mesh of varying sizes. Error bars represent experimental precision and propagation of uncertainty in pore geometry for the observed and predicted fluxes, respectively.

With a single exception, Equation 4.2 over-predicted the oil flux for every mesh size, sometimes by more than an order of magnitude. However, the flux did appear to rise monotonically with an increase in the pore radius, as expected. An unexpected result was the apparent lack of dependence on the coated wire radius. Two meshes, both with the same pore

radius ($r = 55 \mu\text{m}$), but different coated wire radii ($R = 70 \mu\text{m}$ and $R = 167 \mu\text{m}$) had the same observed oil flux of about $0.9 \text{ L}\cdot\text{s}^{-1}\cdot\text{m}^{-2}$ (Figure 4.3, 4th and 5th columns). This observation is in stark contrast to Equation 4.2, which predicts a strong dependency on the coated wire radius. Based on this result, it is very likely that the mesh openings are not cylindrical enough to be modeled as simple capillary tubes with a defined length and radius.

The relationship of the oil flux on mesh geometry was only correctly predicted for a single size. This same mesh ($r = 55 \mu\text{m}$, $R = 167 \mu\text{m}$) was tested with multiple types of oil to study the effect of varying oil viscosity while controlling for the influence of the mesh geometry. That is, any deviations from the model would likely be due to the viscosity term, not the mesh geometry terms. The results from testing four different oils are shown in Figure 4.4.

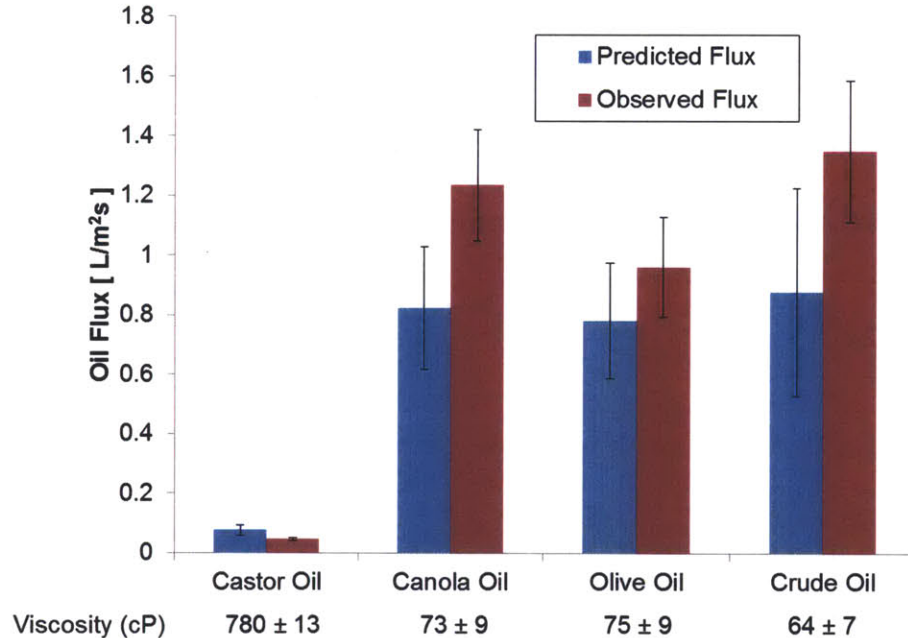


Figure 4.4: Comparison of predicted and observed oil permeate flux through a single mesh with coated dimensions of $r = 55 \mu\text{m}$, and $R = 167 \mu\text{m}$. Coating concentration was $60 \text{ mg LDPE} / \text{mL xylene}$.

For all four oils tested, Equation 4.2 successfully predicted the oil flux to within quantifiable uncertainty. In addition, flux increased monotonically as viscosity increased, again agreeing with the model. The fact that Equation 4.2 works best with this specific mesh size is likely a coincidence useful for testing purposes. However, this phenomenon, that the influence of viscosity is better predicted than the influence of mesh geometry, is a reflection of the nature of flow through small orifices. Even in very non-ideal circumstances, such as blunt orifices and irregular surfaces, flux is generally inversely proportional to viscosity.¹⁰ At these small scales, the flow of homogenous fluids is laminar, and viscosity will be isotropic. As long as the openings have axial symmetry (averaged across all openings), the influence of viscosity on flux will remain consistent, regardless of its magnitude.

Finally, we observed that in all cases the oil permeate had a water content of less than 1% by volume (the detection limit of this method). Since the solubility of water in these oils at room temperature is in the range of 10-500 ppm,¹¹ this indicates that oil flow through the mesh does not induce the passage of free phase water under quiescent conditions.

4.5 Conclusions

The rate of oil percolation through a hydrophobic mesh was tested in a calm environment where capillary-induced flow dominates. Observed fluxes of oil through the hydrophobic mesh are at least an order of magnitude higher than most reported values in the literature, even some driven by larger hydrostatic pressure. The oil permeate has less than 1% water by volume, which is near the saturated concentration of water in oil. Modification of Washburn's equation led to the successful prediction of the influence of viscosity on oil

permeate flux, but tended to over-predict the effects of mesh geometry, often by an order of magnitude. In addition, the coated wire radius was found to have no effect on the flux. Increasing the complexity of the model to better predict the influence of mesh geometry is a challenging endeavor, since there is a large gap in possible approaches between analytical solutions (such as Equation 4.2) and finite difference modeling. For finite difference models, capturing the required level of detail of the rough, rounded pores will be impractical. A much more useful approach would be to generate empirical expressions from fits of data. This will not only provide the information necessary for optimizing the mesh performance, but may provide some insight into the hydrodynamic mechanisms at work.

4.6 References

- (1) Feng, L.; Zhang, Z.; Mai, Z.; Ma, Y.; Liu, B.; Jiang, L.; Zhu, D. *Angew. Chem., Int. Ed.* **2004**, *43*, 2012-2014.
- (2) Wang, S.; Song, Y.; Jiang, L. *Nanotechnology* **2007**, *18*, 015103.
- (3) Pan, Q.; Wang, M.; Wang, H. *Appl. Surf. Sci.* **2008**, *254*, 6002-6006.
- (4) Lee, C.; Johnson, N.; Drelich, J.; Yap, Y. K. *Carbon* **2011**, *49*, 669-676.
- (5) Kota, A.K.; Kwon, G.; Choi, W.; Mabry, J.M.; Tuteja, A. *Nat. Commun.* **2012**, *3*, 1025-1032.
- (6) Su, C.; Xu, Y.; Zhang, W.; Yang, L.; Li, J. *Appl. Surf. Sci.* **2012**, *258*, 2319-2323.
- (7) Reed, M.; Johansen, Ø; Brandvik, P.J.; Daling, P.; Lewis, A.; Fiocco, R.; Mackay, D.; Prentki, R. *Spill Sci. Technol. Bull.* **1999**, *5(1)*, 3-16.
- (8) Washburn, E.W. *Phys. Rev.* **1921**, *17*, 273-283.
- (9) Vazquez, M.; Beggs, H.D. *J. Pet. Technol.* **1980**, *32(6)*, 968-970.
- (10) Miller, E.E.; Miller, R.D. *J. Appl. Phys.* **1956**, *27(4)*, 324-332.

- (11) Barton, A.F.M. *CRC Handbook of Solubility Parameters and Other Cohesion Methods*, 2nd Edition; CRC Press: Boca Raton, 1991; pp 177-183.

Conclusions & Future Work

A hydrophobic mesh was successfully fabricated using steel mesh dip-coated into an LDPE-xylene solution. The thickness and roughness of the coating could be tuned by varying the concentration of dissolved LDPE. In conjunction with a wide selection of steel mesh sizes, a hydrophobic mesh can be fabricated with any desired opening size, wire thickness, and surface roughness. In order to better correlate the surface geometry of the mesh with liquid contact angles (a common measuring technique), it may be possible to vary the roughness of the surface without altering the coating thickness. Adding a poor co-solvent to the LDPE-xylene mixture may increase the roughness of the LDPE coating by promoting precipitation on the mesh surface. This would help disentangle the competing effects of the roughness ratio and the fractional area in contact with the mesh. However, this insight would strictly be a convenience for characterizing the mesh surface. Wetting fluids were shown to persistently wet the mesh, creating a smooth surface with nearly homogenous surface interactions, attenuating the roughness effect.

The development of a tunable system where mesh characteristics could easily be varied enabled further investigations into how those characteristics affect performance metrics relevant to oil spill separation and recovery. An expression was developed that accurately predicted the breakthrough pressure of water. This expression was derived by applying the Young-Laplace equation to an idealized mesh opening, and incorporating an unpinned interface. The mobile interface is only rarely mentioned in the literature for capillary-like pores, but proved key to

explaining breakthrough depths that, according to simple theory, were impossibly large. This model also suggests that breakthrough pressure is insensitive to the local contact angle. If this is accurate, the roughness ratio of the surface not important compared to mesh geometry, even when not persistently wetted by oil. However, it should be noted that all experiments were done under quiescent conditions. Testing that incorporates waves and water velocity should be undertaken to assess any possible influences of dynamic pressure changes.

A capillary-like model was not as successful in predicting the flux of oil permeate. It predicted a strong dependence on the coated wire radius, but none was observed. However, when the effects of mesh geometry were controlled for, the model correctly predicted the effects of varying the oil viscosity to within quantifiable error. One possible explanation is that the pores were too dissimilar to capillaries, invalidating the assumptions behind the Washburn equation. Alternatively, there could be restricted flow on the inner side of the mesh, after the oil exits the pore. This would decrease the flow rate, and cause the model to over-predict. Since flow is mostly gravity-driven at that point, experiments where the orientation of the mesh relative to the vertical is varied should be attempted. Alternative modeling approaches, such as finite difference models, would be impractical due to the level of detail required to accurately capture the rough, irregular pores. Instead, systematic testing should be undertaken, and the dependence of flux on each variable should be found empirically. This will generate useful information, along with data valuable to understanding the actual mechanisms at work.

The sum of these results and observations are useful first-steps toward designing a mesh optimized to recover spilled oil. With regard to pore size, there is a trade-off between oil flux

and water breakthrough. In this simple case, a minimum operational depth can be set as a constraint, followed by an optimization exercise to maximize oil flux. In addition, the coated wire radius was shown to have a significant influence on breakthrough pressure, providing another variable to change, increasing the possible values of r . However, the effect of mesh geometry on oil flux remains poorly understood. Until a systematic study can be undertaken, an accurate assessment of the full oil recovery potential remains unknown.

Nevertheless, other results provide insight into possible ways to implement a field-scale device. The mesh was able to remove oil from the surface of the water faster than it could be replenished by spreading. This indicates that the oil must be brought to the mesh, or vice-versa. Also, while the maximum observed flux of about $1 \text{ L}\cdot\text{m}^{-2}\cdot\text{s}^{-1}$ was quite high compared to other oil/water separation meshes, it must be put into a practical context. The Deepwater Horizon spill released about $0.10 \text{ m}^3\cdot\text{s}^{-1}$ of crude oil from the seabed.¹ Only about 65% of that oil ascended to the surface without being dissolving into the water column.² With the observed flux through these hydrophobic mesh, it would take an area of approximately 60 m^2 to match that spill rate. While this is a large number, it is not infeasible given the resources utilized during the actual spill. For example, the amount of oil in contact with the mesh at a given time could be increased by increasing the depth of oil using booms, or placing the mesh perpendicular to the current and letting the oil build up against it. At the very least, the results do not rule out hydrophobic meshes as a possible oil recovery technique, and further studies are warranted.

References

- (1) Camilli, R.; Di Iorio, D.; Bowen, A.; Reddy, C. M.; Techet, A. H.; Yoerger, D. R.; Whitcomb, L. L.; Seewald, J. S.; Sylva, S. P.; Fenwick, *Proc. Natl. Acad. Sci. U. S. A.* **2011**, *109* (50), 20260-20267.
- (2) Ryerson, T.B.; Camilli, R.; Kessler, J.D.; Kujawinski, E.B.; Reddy, C.M.; Valentine, D.L.; Atlas, E.; Blake, D.R.; de Gouw, J.; Meinardi, S.; Parrish, D.D.; Peischl, J.; Seewald, J.S.; Warneke, C. *Proc. Natl. Acad. Sci. U. S. A.* **2012**, *109*(50), 20246-20253.

Appendix

Table A.1: Dimensions of coated and uncoated meshes used in Chapter 2 and 3, identified by uncoated opening width.

Approximate Uncoated Mesh Opening Size (μm)	Coating Concentration (mg/mL)	Mean Opening Area of Coated Mesh (μm^2)	Mean Effective Pore Radius (μm)	Effective Coated Wire Radius (μm)
100	Uncoated	9030 \pm 480	95.0 \pm 4.2 ^a	58.3 \pm 4.2 ^b
	15 \pm 1	7840 \pm 510	50.0 \pm 1.6	63.2 \pm 4.2 ^b
	30 \pm 2	4600 \pm 1100	38.2 \pm 4.4	67 \pm 11
	60 \pm 4	150 \pm 160	6.9 \pm 3.9	99 \pm 10
220	Uncoated	35000 \pm 1100	187 \pm 4 ^a	128 \pm 4 ^b
	15 \pm 1	33000 \pm 780	103 \pm 1	132 \pm 4 ^b
	30 \pm 2	21700 \pm 980	83.0 \pm 1.9	139 \pm 8
	60 \pm 4	9300 \pm 1200	54.5 \pm 3.4	167 \pm 9
1500	Uncoated	910000 \pm 14000	954 \pm 4 ^a	185 \pm 4 ^b
	15 \pm 1	908000 \pm 14000	538 \pm 4	188 \pm 4 ^b
	30 \pm 2	726000 \pm 13000	481 \pm 4	206 \pm 10
	60 \pm 4	459000 \pm 10000	382 \pm 4	280 \pm 10

^a Actual opening width. ^b Actual wire radius.

Table A.2: Dimensions of coated meshes used in Chapter 3 and 4, identified by mesh dimensions.

Mean Effective Pore Radius (μm)	Effective Coated Wire Radius (μm)	Mean Opening Area of Coated Mesh (μm^2)	Coating Concentration (mg/mL)
4.5 \pm 2.1	27 \pm 14	64 \pm 51	50 \pm 4
7.0 \pm 3.7	55 \pm 22	150 \pm 140	60 \pm 4
29.4 \pm 5.8	49 \pm 20	2700 \pm 1100	60 \pm 4
30.3 \pm 7.3	54 \pm 22	1900 \pm 1100	60 \pm 4
40.1 \pm 9.0	119 \pm 56	4900 \pm 2300	60 \pm 4
40.0 \pm 7.6	110 \pm 40.	5100 \pm 2400	60 \pm 4
54.6 \pm 3.3	71.1 \pm 9.4	9300 \pm 1200	60 \pm 4
55.1 \pm 3.4	167 \pm 24	9100 \pm 1100	30 \pm 2
80 \pm 10	135 \pm 33	20000 \pm 5100	30 \pm 2
121.1 \pm 7.7	89 \pm 12	46000 \pm 5100	15 \pm 1
126.9 \pm 7.1	82.6 \pm 9.6	50600 \pm 5900	30 \pm 2
145.0 \pm 9.2	83.2 \pm 9.9	66100 \pm 8400	60 \pm 4

